ANNUAL REVIEWS

Annual Review of Astronomy and Astrophysics

Tidal Disruption Events

Suvi Gezari[1,2]

[1]Department of Astronomy, University of Maryland, College Park, Maryland 20742-2421, USA; email: suvi@astro.umd.edu

[2]Joint Space-Science Institute, University of Maryland, College Park, Maryland 20742-2421, USA

Annu. Rev. Astron. Astrophys. 2021. 59:21–58

First published as a Review in Advance on April 29, 2021

The *Annual Review of Astronomy and Astrophysics* is online at astro.annualreviews.org

https://doi.org/10.1146/annurev-astro-111720-030029

Keywords

black holes, transients, accretion physics, surveys

Abstract

The concept of stars being tidally ripped apart and consumed by a massive black hole (MBH) lurking in the center of a galaxy first captivated theorists in the late 1970s. The observational evidence for these rare but illuminating phenomena for probing otherwise dormant MBHs first emerged in archival searches of the soft X-ray ROSAT All-Sky Survey in the 1990s, but has recently accelerated with the increasing survey power in the optical time domain, with tidal disruption events (TDEs) now regarded as a class of optical nuclear transients with distinct spectroscopic features. Multiwavelength observations of TDEs have revealed panchromatic emission, probing a wide range of scales, from the innermost regions of the accretion flow to the surrounding circumnuclear medium. I review the current census of 56 TDEs reported in the literature, and their observed properties can be summarized as follows:

- The optical light curves follow a power-law decline from peak that scales with the inferred central black hole mass as expected for the fall-back rate of the stellar debris, but the rise time does not.
- The UV-optical and soft X-ray thermal emission come from different spatial scales, and their intensity ratio has a large dynamic range and is highly variable, providing important clues as to what is powering the two components.
- They can be grouped into three spectral classes, and those with Bowen fluorescence line emission show a preference for a hotter and more compact line-emitting region, whereas those with only HeII emission lines are the rarest class.

Contents

1. INTRODUCTION

Tidal disruption events (TDEs) originated in the late 1970s as a theoretical concept—that of being a dynamical consequence of massive black holes (MBHs) speculated to be at the centers of most galaxies (Hills 1975, Lidskii & Ozernoi 1979). A star's orbit could bring it close enough to the MBH to be disrupted or captured by the black hole, depending on the relative size of the tidal disruption radius to the black hole event horizon. When a star is disrupted outside the event horizon, which for a solar-type star occurs for $M_{\rm BH} \lesssim 10^8\,{\rm M}_\odot$, a luminous flare of radiation is expected from the bound fraction of the tidal debris that falls back onto the black hole, which circularizes to form an accretion disk (Rees 1988, Evans & Kochanek 1989, Phinney 1989, Ulmer 1999). This electromagnetic signal was suggested at the time to be one of the best probes for dormant MBHs lurking in the galaxy centers, when direct dynamical measurements of black hole mass are not feasible.

TDEs also act as a cosmic laboratory to study the real-time formation of an accretion disk and jet. In a TDE, a previously dormant black hole goes through a dramatic transformation, with a sudden new influx of gas, and potentially magnetic flux, available from the disrupted star for accretion. Given that the timescale for fallback and circularization of the stellar debris streams is as short

as months (see Section 3.1), TDEs allow us to witness the process of the assembly of the nascent accretion disk and the launching of any accompanying outflow or jet. Once the accretion process begins, we can also probe the gas density of the inner regions of galaxy nuclei from observations of the photoionization and the interaction of jets and outflows with its circumnuclear environment.

The rate at which stars are destined to be tidally disrupted is well determined by the mass of the central black hole, and the nuclear stellar density and orbital distribution. Analytical and numerical calculations for stars scattering into the MBH loss cone (Frank & Rees 1976), the angular momentum phase-space for which $R_p < R_T$, where R_p is the pericenter of the star's orbit, are in general agreement for a rate that ranges from 10^{-4}–10^{-5} year^{-1} galaxy^{-1} (Magorrian & Tremaine 1999, Wang & Merritt 2004, Brockamp et al. 2011, Stone & Metzger 2016), with rates as high as 10^{-3} year^{-1} galaxy^{-1} in galaxies with steep nuclear density profiles such as nucleated dwarf galaxies (Wang & Merritt 2004) and poststarburst (E+A) galaxies (Stone & van Velzen 2016). The spin distribution of MBHs can also leave an imprint on the TDE rate, especially at masses close to the maximum mass for which the tidal disruption radius is still outside the black hole's event horizon, M_{max}, which increases from $\approx 1 \times 10^8\,M_\odot$ for a nonspinning (Schwarzschild) black hole up to $7 \times 10^8\,M_\odot$ for a maximally spinning (Kerr) black hole, due to the effects of the shrinking event horizon with increasing spin (Beloborodov et al. 1992, Kesden 2012b).

The presence of a binary MBH, as a product of a recent galaxy merger, can also temporarily enhance (suppress) the TDE rate due to the pumping up (ejection) of stars on radial orbits, until the binary MBH's inspiral, and the loss cone is refilled by two-body interactions (Milosavljević & Merritt 2003, Lezhnin & Vasiliev 2016). Finally, we can test for the mere presence of a central black hole by comparing the TDE rates expected for galaxy-mass functions with different galaxy-mass-dependent black hole occupations fractions (Stone & Metzger 2016), which may reveal the formation mechanism of the MBHs themselves (Greene 2012).

Given these sensitivities of the TDE rate to the mass, spin, binarity, and occupation fraction of MBHs, they serve as excellent probes of MBH demographics. Finally, it should be noted that the demographics, internal structure, and evolutionary state of the unlucky stars themselves can be revealed from the timescales and chemical composition of the observed TDEs (Syer & Ulmer 1999, Lodato et al. 2009, MacLeod et al. 2012, Guillochon & Ramirez-Ruiz 2013, Kochanek 2016, Law-Smith et al. 2020, Ryu et al. 2020b). In **Figure 1**, I plot the distinct regions of the parameter space of black hole mass and impact parameter that TDEs can probe, from the disruption of white dwarfs (WDs) by intermediate-mass black holes (IMBHs) to the disruption of red giants by the most massive black holes known.

Despite the strong theoretical motivations for using TDEs to probe MBHs, and the current census of 56 TDEs reviewed here, progress for using TDEs as probes of black hole demographics has been severely hampered by our lack of understanding of the emission mechanism powering TDEs. Indeed, in the past decade, observations of TDEs have outpaced theoretical modeling, with many important aspects of TDE properties yet to be definitively and consistently accounted for with a physically motivated model for the tidal disruption debris and its eventual assembly into an accretion disk. However, the goal of this review is to present our latest understanding of the observed properties of TDEs, with the hopes that a theoretical understanding will soon follow after a global view of the TDE population.

2. OBSERVED CANDIDATES

We are still at a point in the field of TDEs that the well-studied candidates can be listed individually. In **Table 1**, I list the 56 TDE candidates that have been reported in the literature, including the name of the survey that discovered the transient, the waveband of the survey (UV, optical,

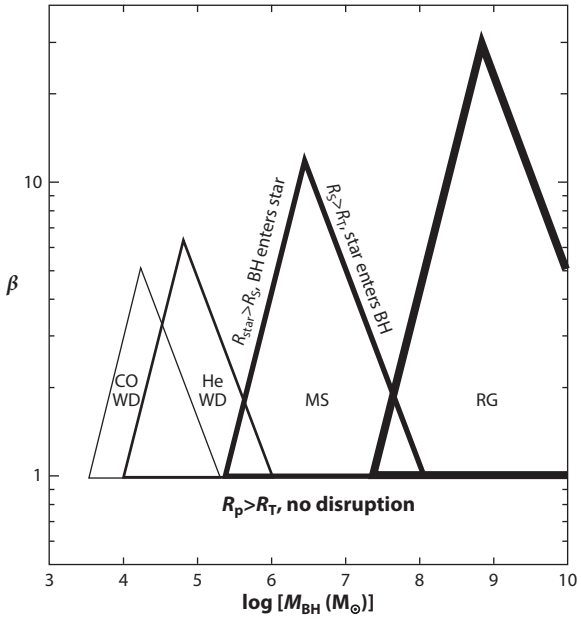

Figure 1

Allowable region for the tidal disruption of stars representative of different evolutionary states, a 0.6-$M_\odot$ CO WD, a 0.17-$M_\odot$ He WD, a 1-$M_\odot$ MS, and a 1.4-$M_\odot$ RG, bounded by the conditions that $R_p < R_T$, $R_\star < R_S$, and $R_T > R_S$ for a TDE to be observable, as a function of M_{BH}, and β is the strength of the tidal encounter ($\beta \equiv R_T/R_p$). Figure inspired by Rosswog et al. (2009). Abbreviations: CO WD, carbon oxygen white dwarf; He WD, helium white dwarf; M_{BH}, black hole mass; MS, main-sequence star; RG, red giant; TDE, tidal disruption event.

X-ray, or gamma-ray), the peak luminosity and the characteristic thermal blackbody temperature at peak, and the reference associated with those measurements. All these nuclear transients have been shown to not harbor an active galactic nucleus (AGN) or a supernova (SN) in the host-galaxy nucleus, with a TDE being the most viable explanation for the flaring source. In principle, TDEs should occur around MBHs that have an AGN accretion disk, and at least one strong candidate has been reported in a narrow-line Seyfert 1 galaxy (Blanchard et al. 2017) and one in a luminous infrared galaxy harboring a dust obscured AGN (Mattila et al. 2018). TDEs in an AGN host may even produce interesting signatures from the interaction of the debris streams with the preexisting AGN disk that could distinguish them from TDEs around quiescent black holes (Chan et al. 2019). However, there are too many ways in which observations of a variable AGN could be mistaken for the signatures of a TDE flare, and so I avoid these candidates to ensure the purity of the TDE census. In **Figure 2**, we show the cumulative number of TDEs reported in the literature as a function of time and color-coded by the survey waveband. Wide-field optical surveys have played an important role in the past decade in discovering TDEs and account for almost two-thirds of all the reported TDEs to date.

One of the most distinguishing characteristics of TDEs is that their continuum is very well described by a thermal blackbody. However, as can be seen in **Figure 2**, the temperature distribution of TDEs is bimodal and seemingly dependent on the waveband in which they were discovered. However, there are now 10 UV-optically selected TDEs for which a soft X-ray component was also detected in follow-up X-ray observations (see Section 3.8). We plot their blackbody temperatures in the figure and see that their characteristic temperatures fall within the X-ray

Table 1 Table of tidal disruption events reported in the literature

Name	Survey[a]	Waveband	Redshift	log L_{BB}[b] (erg s^{-1})	log T_{BB} (K)	Reference[c]
NGC 5905	ROSAT	X	0.01124	40.94	5.84	Bade et al. 1996
RX J1624+75	ROSAT	X	0.0636	43.38	6.05	Grupe et al. 1999
RX J1242-11A	ROSAT	X	0.050	42.60	5.84	Komossa & Greiner 1999
RX J1420+53	ROSAT	X	0.147	43.38	5.67	Greiner et al. 2000
GALEX D3-13	GALEX	U	0.3698	43.98	4.66	Gezari et al. 2006
SDSS J1323+48	XMM	X	0.0875	44.30	5.91	Esquej et al. 2007
GALEX D1-9	GALEX	U	0.326	43.48	4.59	Gezari et al. 2008
TDXF J1347-32	ROSAT	X	0.0366	42.73	6.14	Cappelluti et al. 2009
GALEX D23H-1	GALEX	U	0.1855	43.95	4.70	Gezari et al. 2009
SDSS J1311-01	Chandra	X	0.195	41.74	6.14	Maksym, Ulmer & Eracleous 2010
SwiftJ1644	Swift	G	0.353	ND	ND	Bloom et al. 2011
2XMMi J1847-63	XMM	X	0.0353	42.82	5.96	Lin et al. 2011
SDSS-TDE1	SDSS	O	0.136	43.64	4.42	van Velzen et al. 2011
SDSS-TDE2	SDSS	O	0.2515	44.54	4.37	van Velzen et al. 2011
PS1-10jh	PS	O	0.1696	44.47	4.59	Gezari et al. 2012
SDSS J1201+30	XMM	X	0.146	45.00	6.06	Saxton et al. 2012
SwiftJ2058	Swift	G	1.186	ND	ND	Cenko et al. 2012b
WINGS J1348+26	Chandra	X	0.0651	41.79	6.06	Maksym et al. 2013
PS1-11af	PS	O	0.4046	44.16	4.28	Chornock et al. 2014
RBS 1032	ROSAT	X	0.026	41.70	6.11	Maksym et al. 2014b
PTF-09ge	PTF	O	0.064	44.04	4.08	Arcavi et al. 2014
PTF-09axc	PTF	O	0.1146	43.46	4.08	Arcavi et al. 2014
PTF-09djl	PTF	O	0.184	44.42	4.41	Arcavi et al. 2014
ASASSN-14ae	ASAS-SN	O	0.0436	43.87	4.29	Holoien et al. 2014
3XMM J1521+07	XMM	X	0.179	43.51	6.30	Lin et al. 2015
SwiftJ1112	Swift	G	0.89	ND	ND	Brown et al. 2015
ASASSN-14li	ASAS-SN	O	0.02058	43.66	4.52	Holoien et al. 2016b
ASASSN-15lh	ASAS-SN	O	0.2326	45.34	4.30	Dong et al. 2016
ASASSN-15oi	ASAS-SN	O	0.0484	44.45	4.60	Holoien et al. 2016b
iPTF-16axa	PTF	O	0.108	43.82	4.46	Hung et al. 2017
iPTF-16fnl	PTF	O	0.0163	43.18	4.47	Blagorodnova et al. 2017
3XMM J1500+01	XMM	X	0.1454	43.08	6.06	Lin et al. 2017
OGLE16aaa	OGLE	O	0.1655	44.22	4.36	Wyrzykowski et al. 2017
XMMSL1 J0740-85	XMM	X	0.0173	42.61	6.00	Saxton et al. 2017
iPTF-15af	PTF	O	0.07897	44.10	4.85	Blagorodnova et al. 2019
AT2017eqx/PS17dhz	PS	O	0.1089	43.82	4.32	Nicholl et al. 2019
AT2018zr/PS18kh	PS	O	0.071	43.78	4.14	van Velzen et al. 2021
AT2018bsi/ZTF18aahqkbt	ZTF	O	0.051	43.87	4.53	van Velzen et al. 2021
AT2018dyb/ASASSN-18pg	ASAS-SN	O	0.018	44.08	4.40	Leloudas et al. 2019
AT2018fyk/ASASSN-18ul	ASAS-SN	O	0.059	44.48	4.54	Wevers et al. 2019
AT2018hco/ATLAS18way	ATLAS	O	0.088	44.25	4.39	van Velzen et al. 2021
AT2018hyz/ASASSN-18zj	ASAS-SN	O	0.04573	44.10	4.25	Gomez et al. 2020
AT2018iih/ATLAS18yzs	ATLAS	O	0.212	44.62	4.23	van Velzen et al. 2021

(*Continued*)

Table 1 (*Continued*)

Name	Survey[a]	Waveband	Redshift	log L_{BB}[b] (erg s^{-1})	log T_{BB} (K)	Reference[c]
AT2018lna/ZTF19aabbnzo	ZTF	O	0.091	44.56	4.59	van Velzen et al. 2021
AT2018lni/ZTF18actaqdw	ZTF	O	0.138	44.21	4.38	van Velzen et al. 2021
AT2019ahk/ASASSN-19bt	ASAS-SN	O	0.0262	44.08	4.30	Holoien et al. 2019b
AT2019azh/ASASSN-19dj	ASAS-SN	O	0.0222	44.50	4.51	van Velzen et al. 2021
AT2019bhf/ZTF19aakswrb	ZTF	O	0.1206	43.91	4.27	van Velzen et al. 2021
AT2019cho/ZTF19aakiwze	ZTF	O	0.193	43.98	4.19	van Velzen et al. 2021
AT2019dsg/ZTF19aapreis	ZTF	O	0.0512	44.26	4.59	van Velzen et al. 2021
AT2019ehz/Gaia19bpt	Gaia	O	0.074	44.03	4.34	van Velzen et al. 2021
AT2019eve/ZTF19aatylnl	ZTF	O	0.0813	43.14	4.06	van Velzen et al. 2021
AT2019lwu/ZTF19abidbya	ZTF	O	0.117	43.60	4.14	van Velzen et al. 2021
AT2019meg/ZTF19abhhjcc	ZTF	O	0.152	44.36	4.44	van Velzen et al. 2021
AT2019mha/ATLAS19qqu	ATLAS	O	0.148	44.05	4.35	van Velzen et al. 2021
AT2019qiz/ZTF19abzrhgq	ZTF	O	0.0151	43.44	4.27	van Velzen et al. 2021

[a]Survey that first discovered the nuclear transient.

[b]Integrated blackbody luminosity except for X-ray selected TDEs for which the absorbed luminosity in the 0.3–2-keV band is given.

[c]Publication in which the luminosity and temperature were used.

Abbreviations: ASAS-SN, All-Sky Automated Survey for Supernovae; GALEX, *Galaxy Evolution Explorer*; ND, no data; OGLE, Optical Gravitational Lensing Experiment; PS, Pan-STARRS; PTF, Palomar Transient Factory; SDSS, Sloan Digital Sky Survey; XMM, XMM-*Newton*; ZTF, Zwicky Transient Facility.

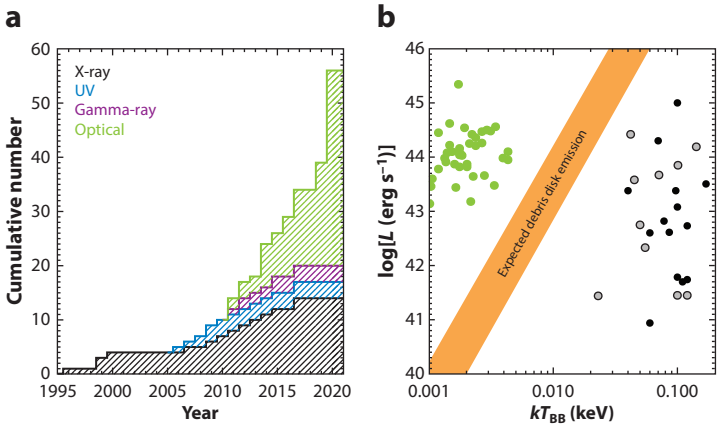

Figure 2

(*a*) Cumulative histogram of TDEs reported in the literature, color-coded by the wavelength in which they were discovered: X-ray (*black*), UV (*blue*), gamma-ray (*purple*), and optical (*green*). (*b*) Peak luminosity versus blackbody temperature for 56 TDEs reported in the literature, color-coded by the wavelength in which they were discovered: UV-optical (*green*), X-ray (*black*), and 10 of the UV-optically selected TDEs with detected X-ray components (*gray*). The UV-optical luminosities are calculated for the entire blackbody, whereas the X-ray luminosities are only for the 0.3–2-keV band but should account for most of the bolometric luminosity given the extremely soft temperatures observed. The region of expected thermal emission from a circularized debris disk formed from the tidal disruption of a solar-type star by a $\sim 10^6$–10^8 $M_\odot$ black hole is shown in orange. Note that neither of the two components are in agreement with emission expected from a simple debris disk.

selected TDE distribution, indicating that these two components are in fact physically distinct. In Section 4.2, we discuss how the UV-optical and X-ray thermal components are related, present an important population of nearby TDEs for which both components have been detected, and reveal clues about their physical natures conjectured from their relative temporal evolution.

2.1. Soft X-Ray Candidates

The first TDE candidates emerged from archival searches of the ROSAT All Sky Survey (RASS) conducted in 1990–1991, whose coverage of 20% of the sky in the 0.1–2.4-keV band, when compared to follow-up pointed observations obtained with the ROSAT Position-Sensitive Proportional Counter (PSPC), revealed luminous ($10^{41–44}$ erg s^{-1}), extremely soft ($\Gamma > 3$) X-ray outbursts from four galaxies with no previous evidence of an AGN, that implied a rate of $\sim 1 \times 10^{-5}$ $year^{-1}$ $galaxy^{-1}$, which is consistent with theoretical dynamical predictions for the rates of TDEs (Donley et al. 2002). Follow-up observations of three of these candidates with the *Chandra X-Ray Observatory* a decade later revealed that they had faded in the X-rays by factors of 240 to 6,000, which is consistent with the expectations of the power-law decline of the accretion rate in a TDE (Halpern et al. 2004).

The next X-ray survey having the wide-field coverage (∼15% of sky) and soft X-ray (0.2–2 keV) sensitivity capable of detecting TDEs was the XMM-*Newton* Slew Survey (XMMSL) starting in 2003, which discovered two galaxies, with no detections in RASS or signs of an AGN in their optical spectra, that were detected as luminous soft X-ray sources in the XMMSL (Esquej et al. 2007) and subsequently shown to have faded in follow-up observations 2–3 years later by a factor consistent with a $t^{-5/3}$ power-law decline (Esquej et al. 2008). However, one of the TDE candidates from XMMSL, NGC 3599, was found to have unanalyzed archival slew observations that showed that the galaxy was bright in the X-rays 18 months before the XMMSL detection and, thus, did not have the flaring behavior of a bona fide TDE (Saxton et al. 2015). More recently, the XMMSL has discovered five more candidates, one of which, XMMSL1 J0740-85, is notable for a well-sampled light curve from follow-up *Swift X-ray Telescope* and pointed XMM-*Newton* observations (Saxton et al. 2017), a detection of a UV-bright transient component from *Swift*/UVOT (UV-Optical Telescope) follow-up, a detection in the radio from a nonrelativistic outflow or a weak jet (Alexander et al. 2017), and a nonthermal $\Gamma \sim 2$ power-law component to the X-ray flare.

A couple more TDE candidates have been discovered by following up archival luminous and extremely soft ROSAT PSPC sources using XMM-*Newton* and/or *Chandra* (Cappelluti et al. 2009, Maksym et al. 2014a), including a candidate from a dwarf galaxy with a central black hole estimated to be $\lesssim 2 \times 10^6$ $M_\odot$ as inferred from the host-galaxy luminosity (Maksym et al. 2014a). A more recent cross match of sources that were detected by RASS, but then had faded in serendipitous XMM-*Newton* observations taken two decades later, revealed three more sources broadly consistent with a TDE, potentially implying a TDE rate of $\sim 3 \times 10^{-5}$ $year^{-1}$ $galaxy^{-1}$ but with no optical spectroscopic follow-up observations to investigate the nature of their host galaxies (Khabibullin et al. 2014).

Several soft X-ray outbursts were also detected from archival searches of *Chandra* data, particularly of rich galaxy clusters with multiple epochs of observations. These include a TDE candidate in a dwarf galaxy, WINGS J1348+26 in cluster Abell 1795 (Maksym et al. 2013), with a host-galaxy stellar mass indicating a black hole in the IMBH range of $1–5 \times 10^5$ $M_\odot$ (Maksym et al. 2014b), and a serendipitous detection of the flare in the extreme-UV (EUV) by the *Extreme Ultraviolet Explorer* (EUVE) satellite (Donato et al. 2014). The large-amplitude, flaring soft X-ray source 3XMM J1521+07 was discovered in archival *Chandra* and XMM-*Newton* observations of a galaxy group, NGC 5813, and identified as a TDE candidate, albeit with a very shallow decline rate postpeak, argued to be the signature of slow circularization and super Eddington accretion (Lin et al. 2015).

Although all the candidates from X-ray observations are convincing because of their extremely soft, thermal X-ray spectra and large variability amplitudes, which are distinct from AGN, one of the weaknesses of these candidates is the lack of high-cadence coverage of the X-ray light curves and multiwavelength coverage to better constrain the broadband spectral energy distributions (SEDs) of the flares. Fortunately, optical surveys have played an important role in enabling prompt discovery and follow-up, as well as have a great improvement in time sampling of days instead of years.

2.2. UV Candidates

The first TDE candidate from UV observations was reported by Renzini et al. (1995) from archival *Hubble Space Telescope* (HST)/Faint Object Camera (FOC) observations of elliptical galaxy NGC 4552, which showed an enhanced nuclear flux in an epoch in 1993 compared to 1991. However, HST/Faint Object Spectrograph (FOS) follow-up spectroscopy by Cappellari et al. (1999) found broad line emission from the nucleus, indicative of a low-luminosity AGN.

The first search for TDEs in UV survey data was done with the *Galaxy Evolution Explorer* (GALEX) Deep Imaging Survey (DIS), which surveyed a total of 80 deg^2 of sky in the *NUV* and *FUV* bands in order to produce deep UV images to map the star-formation history of galaxies out to $z \sim 2$ (Martin et al. 2005). A systematic search for extragalactic UV transients from creating yearly coadds of the multiple exposures taken to build up the GALEX DIS images, and selecting only host galaxies with follow-up optical spectra that indicated an inactive galaxy host, yielded three candidates, two of which, D1-9 and D3-13, were serendipitously detected as an optical transient in g, r, i, and z-band difference imaging from the Canada-France-Hawaii Telescope (CFHT) Legacy Survey (CFHTLS) (Gezari et al. 2006, 2008, 2009). The third GALEX candidate, D23H-1, was followed up with prompt optical imaging that detected a coincident optical transient (Gezari et al. 2009); however, this candidate is now suspect, because a significant level of variability was detected in the mid-infrared (MIR) 2–7 years after the peak from serendipitous *Wide-Field Infrared Survey Explorer* (WISE) observations, which suggest that the event could be associated with persistent variability of an AGN (van Velzen et al. 2016), which was masked by the strong emission lines powered by star formation in the host-galaxy spectrum (Gezari et al. 2009).

The multiband detections of these TDE candidates in the *FUV*, *NUV*, g, r, i, and z bands were well fitted by thermal blackbody emission, although with blackbody temperatures an order of magnitude cooler than had been measured for the X-ray-selected TDEs with $T_{\rm BB} \sim (5–6) \times 10^4$ K and $L_{\rm BB} \sim (4–6) \times 10^{43}$ erg s^{-1} (Gezari et al. 2009). *Chandra* follow-up X-ray observations of the GALEX TDE candidates, 1–2 years after their UV-optical peak, revealed weak, extremely soft X-ray emission in D1-9 and D3-13 (Gezari et al. 2008), indicating a second, higher-temperature component [$T_{\rm BB} \sim (3–5) \times 10^5$ K], distinct from the UV-optical thermal emission (Gezari et al. 2009).

Although the UV light curves constructed from GALEX DIS images with a yearly cadence were consistent with a flaring event, the optical light curves extracted from CFHTLS with a much higher cadence of 4 days were in remarkably good agreement with numerical simulations for the fallback rate expected in a TDE, albeit with evidence for a shallower decline rate at late times (Gezari et al. 2009). Furthermore, the optical difference imaging from CFHTLS localized the position of the flares to within 0.25 arcsec of the host-galaxy nucleus, which was a great improvement over the 5-arcsec GALEX point-spread function. The detection of TDEs in optical survey data, designed for the detection of SNe, had powerful implications for the next generation of optical surveys, such as Panoramic Survey Telescope & Rapid Response System (Pan-STARRS) and Palomar Transient Factory (PTF), to detect large numbers of TDEs and to do so in real-time.

2.3. Optical Candidates

Before the first real-time searches for TDEs from optical time domain data, van Velzen et al. (2011) performed an archival study of the 300-deg^2 Sloan Digital Sky Survey Stripe 82 survey with the 2.5-m telescope at Apache Point Observatory multiepoch data to search for nuclear transients in inactive galaxy hosts. This search yielded two candidates, TDE1 and TDE2, which had serendipitous UV detections by GALEX, and again were well described by thermal emission with $\sim 2 \times 10^4$ K and a light curve that could be fitted with a power-law decline, although the decline was shallower than the $t^{-5/3}$ decline expected for the fallback rate. TDE2 had a serendipitous follow-up spectrum during the flare, which showed evidence of transient broad Hα emission associated with the event. One of the most important results of this study was that the properties of the optical light curve, namely their blue optical color, and lack of color evolution with time could be used to distinguish TDEs from more common interlopers like variable AGNs and SNe. This study also measured an empirical TDE rate of 1.9 year^{-1} (Ω/300 deg^2) ($m_{\rm lim}$/22 mag)$^{-3/2}$, which could be scaled to the flux limit ($m_{\rm lim}$) and area (Ω) of future optical surveys.

There was a huge jump in the quality of TDE light curves with the search for TDEs in real time from optical time domain surveys. PS1-10jh was the first TDE detected with a well-sampled rise to peak in optical survey data and was discovered in a joint search by Gezari et al. (2012) for nuclear transients in the 2-day cadence GALEX Time Domain Survey in the *NUV* and the 3-day cadence *g*-, *r*-, *i*-, and *z*-band optical difference imaging of the 70-deg^2 Pan-STARRS1 (PS1) Medium Deep survey (MDS) taken with the 1.8-m telescope at the Haleakala Observatory (Chambers et al. 2016). **Figure 3** shows the well-sampled GALEX+PS1 light curve of PS1-10jh, including a late-time *NUV* detection from HST/WFC3 (Wide-Field Camera 3; Gezari et al. 2015), and a fit to a numerical simulation for the fallback rate in a TDE from Guillochon & Ramirez-Ruiz (2013). The light curve is distinct from a SN for its remarkably constant blue optical color and persistent UV-bright emission, and it is surprising how well the numerical simulations describe

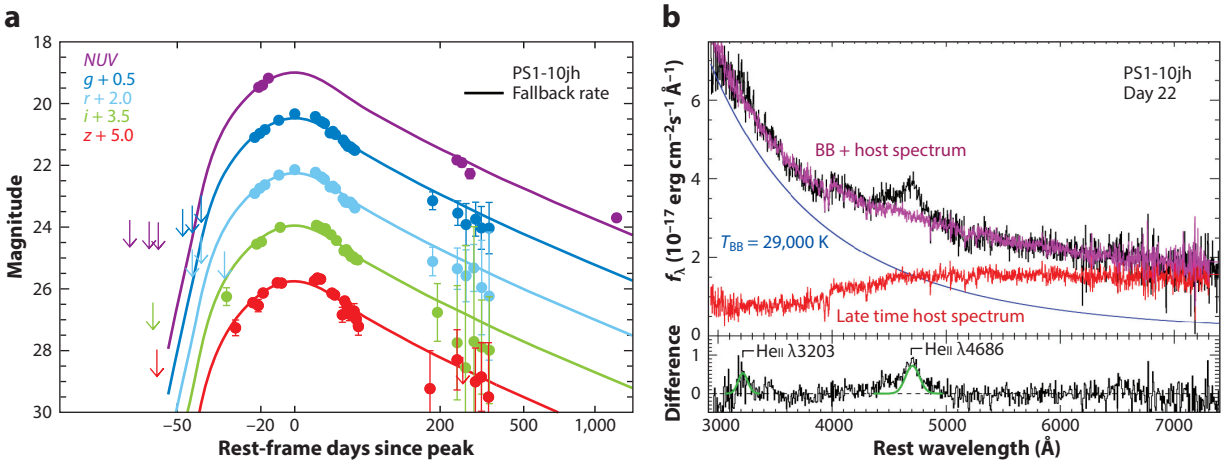

Figure 3

(*a*) GALEX Time Domain Survey *NUV* and Pan-STARRS1 Medium Deep Survey optical *g*, *r*, *i*, and *z* light curve of TDE PS1-10jh, with a late-time detection by HST/WFC3 in the *NUV*. Lines show a numerical simulation for the fallback rate in a TDE scaled to fit the light curve. (*b*) Detection of transient, broad HeII line emission on top of the hot, thermal continuum 22 days before the peak of the flare in TDE PS1-10jh. Panel *a* adapted from Guillochon & Ramirez-Ruiz (2013) with permission, and panel *b* from Gezari et al. (2015). Abbreviations: HST/WFC3, *Hubble Space Telescope*/Wide-Field Camera 3; GALEX, *Galaxy Evolution Explorer*; Pan-STARRS1, Panoramic Survey Telescope & Rapid Response System 1.

the light curve shape, with no additional physics added to account for accretion physics or radiative transfer effects.

Another important aspect of this event was the first unambiguous detection of transient, broad emission lines in prompt optical spectroscopic follow-up observations. Interestingly, the most prominent broad spectral feature in PS1-10jh was misidentified as MgII λ2800 at $z \sim 1$. However, when the transient faded enough to reveal the underlying host-galaxy absorption features 7.5 months after peak at $z = 0.1696$, the broad line in the peak spectrum was identified as HeII λ4686 with FWHM = 9,000 km s^{-1}, along with a detection of broad HeII λ3203, and no detection of broad Balmer line emission, which it would be expected to have (see **Figure 3**). A careful subtraction of a late-time spectrum of the host galaxy placed further limits on the HeII/Hα ratio to be >5 in the prepeak spectrum (Gezari et al. 2015). This first spectroscopic TDE was to be the first of a rare class of helium-only TDEs (TDE-He).

A second TDE candidate, PS1-11af (Chornock et al. 2014), was discovered from a search for blue, UV-bright nuclear transients in the GALEX and PS1 data; this TDE was similar in UV-optical blackbody temperature and light curve shape to the other UV-optical TDEs. This higher-redshift TDE, at $z = 0.4046$, was notable for having a relatively featureless spectrum, except for transient broad absorption features in the UV at early times, which was reminiscent of the OII "W" feature seen in some superluminous supernovae (SLSNe), but without the emergence of any optical-line features or significant cooling, as seen in SLSNe.

Pan-STARRS has continued surveying the Northern Sky in the wide optical filter that spans the *g*, *r*, and *i* bands as the Pan-STARRS Survey for Transients. From this survey has come the discovery of AT2017eqx/PS17dhz, which had a typical UV-optical light curve of a TDE but demonstrated the first case of a transformation in TDE spectral class, from a TDE-H+He to TDE-He spectrum, with initially broad H and HeII lines and with the broad H lines disappearing on a timescale of ∼100 days (Nicholl et al. 2019). We note that this is the first TDE for which there is both a survey name and an astronomical transient (AT) name (assigned by the Transient Name Server or TNS). The TNS AT name is the official International Astronomical Union (IAU) mechanism for reporting new ATs and is important for keeping track of transients that are increasingly being detected by multiple surveys. It is the convention to assign the survey name from the survey that first registered the coordinates of the transient with the TNS.

An archival analysis of transients in the PTF survey with the Palomar 48-in telescope, with follow-up spectra and peak absolute magnitudes intermediate between SNe Ia and SLSNe (−19 mag < M_R < −21 mag), produced three nuclear transients, one of which, PTF 09ge, had a very similar light curve shape and HeII-only spectrum to that of PS1-10jh (Arcavi et al. 2014). The other two, PTF09djl and PTF09axc, had less well-sampled light curves but did show very broad Balmer line features, representing a class of H-rich TDEs (TDE-H), and interestingly, had strong Hδ absorption that is characteristic of the rare class of E+A galaxies, whose strong A-star features and no emission lines are explained as poststarburst galaxies with a truncation of star formation ∼1 Gyr ago. PTF had detected another interesting blue, nuclear transient, PTF10iya, in a star-forming galaxy (Cenko et al. 2012a); however, with its poorly sampled light curve, featureless optical spectrum, and nonthermal X-ray spectrum ($\Gamma \sim 2$), the association of the short-lived (∼10 days) event with a TDE was not clear-cut.

A real-time search for TDEs was conducted during the next phase of PTF operations, known as iPTF. During this search, the strategy for selecting TDEs was to use complete *Neil Gehrels Swift* UV follow-up of all nuclear transients to filter out AGN and SNe. This systematic UV follow-up program that, due to finite *Swift* observing time, was limited to nuclear transients in red galaxy hosts (characteristic of previous TDE discoveries) yielded three more nuclear transients with properties consistent with previously discovered optical TDEs: iPTF-16axa (Hung et al.

2017), iPTF-16fnl (Blagorodnova et al. 2017), and iPTF-15af (Blagorodnova et al. 2019). At the time, iPTF-16fnl was the closest optical TDE ever detected, notably in a nearby E+A galaxy at $z = 0.0163$, and with a lower peak luminosity ($L_{BB} \sim 10^{43}$ erg s^{-1}) and faster fading timescale than previous TDEs, which have important implications for the TDE luminosity function and rate. An HST/STIS (Space Telescope Imaging Spectrograph) UV spectrum of iPTF-15af revealed broad absorption and emission-line features analogous to broad absorption line quasars (BALQSOs), suggesting the presence of an outflow; this is discussed further in Section 3.9.

One of the unexpected results from the All-Sky Automated Survey for Supernovae (ASAS-SN) survey (Kochanek et al. 2017), a network of 14-cm telescopes hosted by the Las Cumbres Observatory, is that despite its large pixel size (8 arcsec) compared to other optical surveys, the survey is highly efficient in detecting TDEs in the nuclei of galaxies. Important reasons for this are the bright limit of ASAS-SN ($m < 17$ mag) and the manageable detection rate, allowing for near spectroscopic completeness (Brown et al. 2019) and, thus, no selection bias in spectroscopically following-up and classifying transients. In the first two years of the ASAS-SN survey, they discovered four TDEs: ASASSN-14ae (Holoien et al. 2014), ASASSN-14li (Holoien et al. 2016b), ASASSN-15lh (Dong et al. 2016, Leloudas et al. 2016), and ASASSN-15oi (Holoien et al. 2016a). The bright, nearby TDEs discovered by ASAS-SN allow for high signal-to-noise multiwavelength follow-up and spectroscopic monitoring. We discuss each of these important TDE discoveries as we discuss the exciting results from their multiwavelength observations below, including detections in the X-ray, MIR, and radio wavelengths.

In the past two years, ASAS-SN has discovered another five TDEs (AT2018fyk/ASASSN-18ul, AT2018dyb/ASASSN-18pg, AT2018hyz/ASASSN-18zj, AT2019ahk/ASASSN-19bt, and AT2019azh/ASASSN-19dj). ASAS-SN has an impressive discovery rate that is only recently being outpaced by the Zwicky Transient Facility (ZTF) survey. One of these recent TDE discoveries, AT2019ahk/ASASSN-19bt, was detected in the *Transiting Exoplanet Survey Satellite* (TESS) Continuous Viewing Zone (CVZ), which enabled the extraction of a light curve in the TESS broadband optical filter binned into a cadence of just 2 h over a timescale of 2 months (Holoien et al. 2019a)! This allowed for an extremely detailed look at the prepeak light curve of the TDE, which was surprisingly smooth and well fitted to an $\propto t^2$ rise to peak in the first 15 days of its 41-day rise to peak.

The ZTF (Bellm et al. 2019), which uses an upgraded detector on the Palomar 48-in telescope with a 50-deg^2 field of view and a limiting magnitude per epoch of $m_{lim} \sim 20.5$ mag in the g and r bands, as well as a dedicated robotically operated low-resolution ($R \sim 100$) SED machine (SEDM) spectrograph on the Palomar 60-in telescope (Blagorodnova et al. 2018) for classification of transients brighter than 19 mag, has yielded the largest sample of TDEs from a single survey to date. In the first 1.5 years of survey operations, they reported the systematic selection, classification, and characterization of 17 TDEs (van Velzen et al. 2021), some of which were detected or discovered by other surveys, including ASAS-SN, the Asteroid Terrestrial-impact Last Alert System (ATLAS; Tonry et al. 2018), and the Pan-STARRS Survey for Transients (Nicholl et al. 2019).

2.4. Hard X-Ray Candidates

There was a big shift in the TDE landscape on March 25, 2011, when *Swift*/BAT (Burst Alert Telescope) discovered a long-duration hard X-ray transient, accompanied by transient radio and IR emission, from the nucleus of a quiescent galaxy at $z = 0.3543$: Swift J1644+57 (Bloom et al. 2011, Levan et al. 2011, Zauderer et al. 2011). The hard, power-law X-ray spectrum, highly super-Eddington luminosity (isotropic X-ray luminosity of $\sim 10^{47}$ erg s^{-1}), radio synchrotron spectrum, and power-law decline of the X-ray light curve were explained as having viewed an on-axis collimated jet launched by the tidal disruption of a star by the galaxy's central $\sim 10^6$-$M_\odot$ black hole. In

fact, a class of jetted TDEs had been predicted by Giannios & Metzger (2011), but their models focused on off-axis emission from the interaction of the jet with the interstellar medium (ISM), and radio searches had only yielded a few late-time detections (Bower 2011, Bower et al. 2013), implying that ∼10% of TDEs launch jets. Two more jetted TDE candidates were detected by *Swift* with similar X-ray and radio properties: Swift J2058+05 (Cenko et al. 2012b, Pasham et al. 2015) and Swift J1112-82 (Brown et al. 2015). The implied rate of jetted TDEs is only $\sim 3 \times 10^{-10}$ year^{-1} galaxy^{-1}, suggesting a combination of the effects of a small beaming angle (∼1 deg), and that only ∼10% of TDEs produce relativistic jets (Brown et al. 2015).

In the case of Swift J2015+05, a thermal component ($T_{\rm BB} \sim 3 \times 10^4$ K) in the UV and optical was detected (similar to the UV and optically selected TDEs) that may have been missed in Swift J1644+57 due to dust extinction in the host-galaxy nucleus. A systematic search of 53,000 galaxies within 100 Mpc using observations in the *Swift*/BAT archive yielded the association of a hard X-ray flare from nine quiescent galaxies, implying a candidate TDE rate in the hard X-rays of 2×10^{-5} year^{-1} galaxy^{-1}. This is a rate comparable with that measured for TDEs selected in the soft X-rays and suggests that hard X-ray components could be ubiquitous even in unbeamed TDEs (Hryniewicz & Walter 2016). However, with sparsely sampled X-ray light curves, and no multiwavelength follow-up data, it is hard to verify their classification as bona fide TDEs.

International Gamma-Ray Astrophysics Laboratory (INTEGRAL) discovered a flaring hard X-ray source in the 20–40 keV band, which was also detected in the 2–10 keV band in follow-up observations with *Swift* and XMM-*Newton*, from the nucleus of the nearby spiral galaxy NGC 4845, which was believed, on the basis of X-ray spectrum, luminosity, and timing arguments, to be emission from an accretion disk corona formed from the tidal disruption of a super-Jupiter-sized object around a $\sim 3 \times 10^5$-$M_\odot$ black hole (Nikołajuk & Walter 2013) and was also detected as a radio transient consistent with emission from an off-axis jet (Lei et al. 2016). The tidal disruption of a substellar object was also invoked to explain the low peak luminosity of the ROSAT soft X-ray-selected TDE in NGC 5905 (Li et al. 2002).

3. OBSERVED PROPERTIES

It is now possible, with the growing census of observed TDEs listed above, to compare them in detail to the theoretical expectations for emission from TDEs and attempt to extract the physical parameters of the events, including black hole mass and stellar type. However, as we discuss below, there are many discrepancies between the observations and the basic predictions for emission from an accreting debris disk, requiring important modifications to the simplest emission models.

3.1. Light Curves

The tidal disruption of a star occurs when it approaches the distance from the black hole at which the tidal forces exceed the self-gravity of the star,

$$\frac{GMR_\star}{r^3} > G\frac{M_\star}{R_\star^2}, \qquad 1.$$

resulting in a tidal disruption radius,

$$R_{\rm T} = R_\star \left(\eta^2 \frac{M_{\rm BH}}{M_\star}\right)^{1/3}, \qquad 2.$$

where $\eta \simeq 1$ and depends weakly on the structure of the star (Evans & Kochanek 1989, Phinney 1989). After disruption, the stellar debris has a spread of specific binding energy,

$$\Delta\epsilon = \pm\frac{GM_\star}{R_{\rm T}^2}R_\star = \frac{GM_\star}{R_\star}\left(\frac{M_{\rm BH}}{M_\star}\right)^{1/3}, \qquad 3.$$

such that half the mass is gravitationally bound to the black hole ($\Delta\epsilon < 0$) and, thus, available to be accreted. The fallback timescale ($t_{\rm fb}$), the characteristic minimum timescale in a TDE, is defined as the orbital period of the most bound debris,

$$t_{\rm fb} = 2\pi G M_{\rm BH}(2E)^{-3/2} = \frac{\pi}{M_\star}\left(\frac{M_{\rm BH}R_\star^3}{2G}\right)^{1/2} = 0.11\ {\rm year}\ r_\star^{3/2}M_6^{1/2}m_\star^{-1}. \quad 4.$$

The fact that $t_{\rm fb}$ scales with the square root of the black hole mass implies that the timing of TDE flares should in principle be used to yield information on the mass of the central black hole. Another fundamental property of the fallback of the debris streams is that if their specific energy distribution is uniform, i.e., $dE/dM = 0$, then the rate at which material returns to pericenter can be derived as

$$\frac{dM}{dE}\frac{dE}{dt} = \frac{2\pi}{3}(GM_{\rm BH})^{2/3}\frac{dM}{dE}t^{-5/3} \quad 5.$$

and follows a power law, $dM/dt \propto (t - t_{\rm D})^{-5/3}$. In the case of a partial disruption, a steeper power-law decline is expected, $dM/dt \propto (t - t_{\rm D})^{-9/4}$ (Coughlin & Nixon 2019). In addition, the internal structure (Ramirez-Ruiz & Rosswog 2009, Guillochon & Ramirez-Ruiz 2013, Golightly et al. 2019b) and spin (Golightly et al. 2019a) of the star, as well as the spin of the black hole (Kesden 2012b, Gafton & Rosswog 2019) and the impact parameter of the star's orbit (Gafton & Rosswog 2019), will have an imprint on the energy distribution of the debris and, thus, the fallback rate.

One of the most remarkable observed characteristics of TDEs is that, at face value, they appear to have a light curve that follows the general shape of the theoretical TDE fallback rate (**Figure 4**). In fact, when one fits a $t^{-5/3}$ power law to the light curve on its decline from peak, there is a strong correlation between the time of peak since the inferred time of disruption, $\Delta t = (t_{\rm peak} - t_{\rm D})$, and

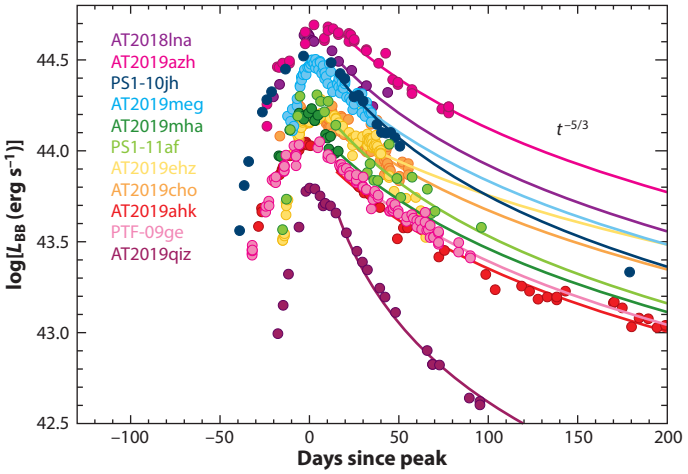

Figure 4

Compilation of bolometric luminosity curves of TDEs with well-sampled prepeak optical light curves, labeled by their AT name, with the exception of PS1-10jh, PS1-11af, and PTF-09ge. The light curves were constructed by scaling the *r*-band light curve by the peak bolometric luminosity determined from a blackbody fit to the optical+UV photometry reported by van Velzen et al. (2020) and assuming no evolution in temperature. In the case of PTF-09ge, no UV observations were taken at the time of the event, and so the bolometric luminosity is estimated from its optical spectrum. In the case of AT2019ahk/ASASSN-19bt, I plot the *Swift uvw2* light curve scaled by the peak bolometric luminosity. Also shown is a $t^{-5/3}$ power-law decline fit to these curves after peak. Abbreviation: AT, astronomical transient.

the estimated black hole mass, where $\Delta t \propto M_{\rm BH}^{1/2}$, as would be expected for the fallback timescale (van Velzen et al. 2019, 2020).

However, this good agreement between the optical light curves and the $t^{-5/3}$ power law of the fallback accretion rate is not entirely consistent with the theory. For emission from a geometrically thin, and optically thick, accretion disk, one would expect a gradual cooling over time with the declining accretion rate, because $T_{\rm disk} \propto \dot{M}^{1/4}$. Thus for optical emission, which is on the Rayleigh Jeans tail of the hot blackbody emission characteristic of TDEs, $\nu L_\nu \propto T \propto \dot{M}^{1/4} \propto t^{-5/12}$ (Lodato & Rossi 2011), and one expects a shallower power-law in the optical bands. Furthermore, there does not appear to be a strong correlation between the rise time to peak and black hole mass (van Velzen et al. 2021), as one would expect if it was following the fallback rate. Regardless, the fact that the observed light curve decline follows the fallback rate is still somewhat of a surprise, given that this assumes that the accretion rate is equivalent to the fallback rate, which allows for no time delay for the debris streams to shock and circularize into an accretion disk. The physical implication is that either accretion does proceed promptly or we are seeing emission from a process not related to the accretion disk but potentially from the debris stream collisions themselves. One of the important ways to distinguish between these scenarios is by looking at the evolution of the soft X-ray emission in these events, which are a more direct tracer of the accretion flow near the central black hole. These are discussed in more detail in Section 4.2.

3.2. Peak Luminosities and Characteristic Temperatures

The peak fallback rate, $\dot{M}_{\rm peak} \sim \frac{1}{3}\frac{M_\star}{t_{\rm fb}}$, results in a range of Eddington ratios, depending on the central black hole mass and the fraction of gas expelled in an outflow ($f_{\rm out}$),

$$\frac{\dot{M}(t_{\rm fb})}{\dot{M}_{\rm Edd}} = 133(\eta/0.1)M_6^{-3/2}m_\star^{4/5}(1-f_{\rm out}), \qquad 6.$$

where $L_{\rm Edd} = \eta \dot{M}_{\rm Edd} c^2 = 1.3 \times 10^{44} M_6$ erg s^{-1}. This presents the possibility that the mode of the accretion flow will be vastly different for black holes of different mass, with black holes being less than 3×10^7 M$_\odot$ in the super-Eddington regime and above 3×10^7 M$_\odot$ in the sub-Eddington regime (Strubbe & Quataert 2009, Lodato & Rossi 2011, Metzger & Stone 2016). This Eddington limit should imprint itself on the TDE luminosity function if nonaxisymmetric effects are not dominant. The estimation of the Eddington ratio requires a measurement of the central black hole mass. For the two dozen TDEs with host-galaxy velocity dispersion measurements used to estimate $M_{\rm BH}$, the inferred Eddington ratios appear to be clustered between ~0.1–1 for the UV-optical component and to have a much larger range for the soft X-ray component, i.e., ~10^{-3}–1 during peak (Wevers et al. 2019). However, given the dramatic variability observed in X-rays from TDEs, as discussed in Section 3.8, there could be many factors contributing to the low Eddington ratios of the X-ray component in some cases, including the presence of obscuration, delayed accretion, and nonisotropic emission.

By combining the observed luminosities with the flux limits of the individual surveys, van Velzen (2018) calculated a luminosity function for TDEs fitted by a power law, $dN/dL \propto L^{-2.5}$, with no correlation with black hole mass, as would be expected for Eddington-limited accretion. However, van Velzen (2018) explains this as a potential result of the sensitivity of $\dot{M}_{\rm fb}$ to $M_\star$. Because $\dot{M}_{\rm fb} \propto M_\star^{4/5}$ (see Equation 6), then for an initial mass function of stars, where $dN_\star/dM_\star \propto M_\star^{-\alpha}$, where $\alpha \sim 2.3$, one would expect a steep decrease of the event rate with peak luminosity. However, there may be other effects on the peak luminosity, such as photon trapping in a radiatively driven wind, which we address in Section 4.3.

3.3. Spectral Classes

The first definitive detection of transient line emission from a TDE was reported for PS1-10jh (Gezari et al. 2012). This TDE was selected as a UV-bright, optically blue nuclear flare in a galaxy with an unknown redshift. Its spectrum, taken 3 weeks before its peak, delayed the classification of the event as a TDE, because on top of the very blue continuum, only a single strong broad emission line was detected and assumed to be MgII λ2798. This line has been seen in isolation in the optical spectra of higher-redshift quasars ($1 \lesssim z \lesssim 1.5$) for which the Hβ line has been redshifted out of the optical band. It was not until the flare faded enough for the absorption features of the host galaxy to emerge at $z = 0.1696$ that the broad line detected in the spectrum was identified as HeII λ4686, a line predicted by Ulmer (1999) to be a signature of the hot photoionizing continuum in a TDE. In fact, transient, broad HeII emission had been detected in a Seyfert galaxy, NGC 5548, and interpreted as the accretion of new material, at small distances from the black hole, potentially from the tidal disruption of a star (Peterson & Ferland 1986).

Although the detection of HeII λ4686 fit into the expectations of a TDE spectrum, the complete lack of any H features was very surprising; however, this confirmed that the gas being photoionized by the event was not ambient gas from the ISM but originated from the stellar debris itself. The high HeII λ4686/Hα ratio was explained as either a signature of He-rich gas from the tidal disruption of a stripped star (Gezari et al. 2012, Bogdanović et al. 2014) or the result of suppression of H line emission due to optically thick reprocessing (Roth et al. 2016). Soon after, archival detections of three new optical TDE candidates were reported by the PTF survey; the one for which they had the best-sampled light curve, PTF09ge, also showed only broad HeII line emission in its spectrum (Arcavi et al. 2014)! However, two of the PTF TDE candidates showed only broad H Balmer line emission, and the first TDE from the ASAS-SN survey, ASASSN-14ae (Holoien et al. 2014), showed both H and HeII features, leading Arcavi et al. (2014) to suggest a continuum of spectral types, from H-dominated to intermediate H+He to He-dominated spectra.

This continuum of spectral classes became more complex with the identification of Bowen fluorescence metal lines of OIII λ3760 and NIII λ4100 and λ4640 in the intermediate H+He spectral-type TDEs, e.g., iPTF15af (Blagorodnova et al. 2019), and in ASASSN-14li, iPTF16axa, and AT2018dyb/ASASSN-18bg (Leloudas et al. 2019, Holoien et al. 2020). Interestingly, despite these lines being expected in systems with strong UV radiation (λ < 228 Å), Bowen fluorescence lines had only recently been detected in AGN spectra in a new class of flaring AGN by Trakhtenbrot et al. (2019). This trend was further strengthened by the detection of these OIII and/or NIII features in all of the H+He TDEs from the ZTF survey (seven classified as TDE-H+He), with the remaining TDEs having either only broad H features (nine classified as TDE-H) or broad HeII features (one classified as TDE-He) (van Velzen et al. 2021). Indeed, HeII λ4686 is expected to accompany Bowen lines, because the Bowen fluorescence mechanism is triggered by the ionization and recombination of HeII (Leloudas et al. 2019), which excites transitions in N and O with similar energies to that of the HeII Lyα photons (Bowen 1935). However, Leloudas et al. (2019) note that not all TDEs with strong HeII lines exhibit the Bowen fluorescence lines, suggesting that they do not all have the optimal physical conditions for strong resonance to happen. However, in fact, in the ZTF TDE sample, all TDEs with H and HeII lines show Bowen features, whereas only the spectra having HeII exclusively do not have Bowen features.

Van Velzen et al. (2021) presented a suggestive trend that spectral type correlates with the radius and temperature of the UV-optical photosphere, with TDE-Bowen spectra coming from smaller radii (i.e., a more compact region) and higher temperatures, both physical conditions that are more conducive to powering Bowen fluorescence, than that for the H-rich spectra. In **Figure 5**, I plot the luminosity below 228 Å versus radius for the optically selected TDEs as a function of their spectral class. The TDE-H+He class (including Bowen line features) clearly

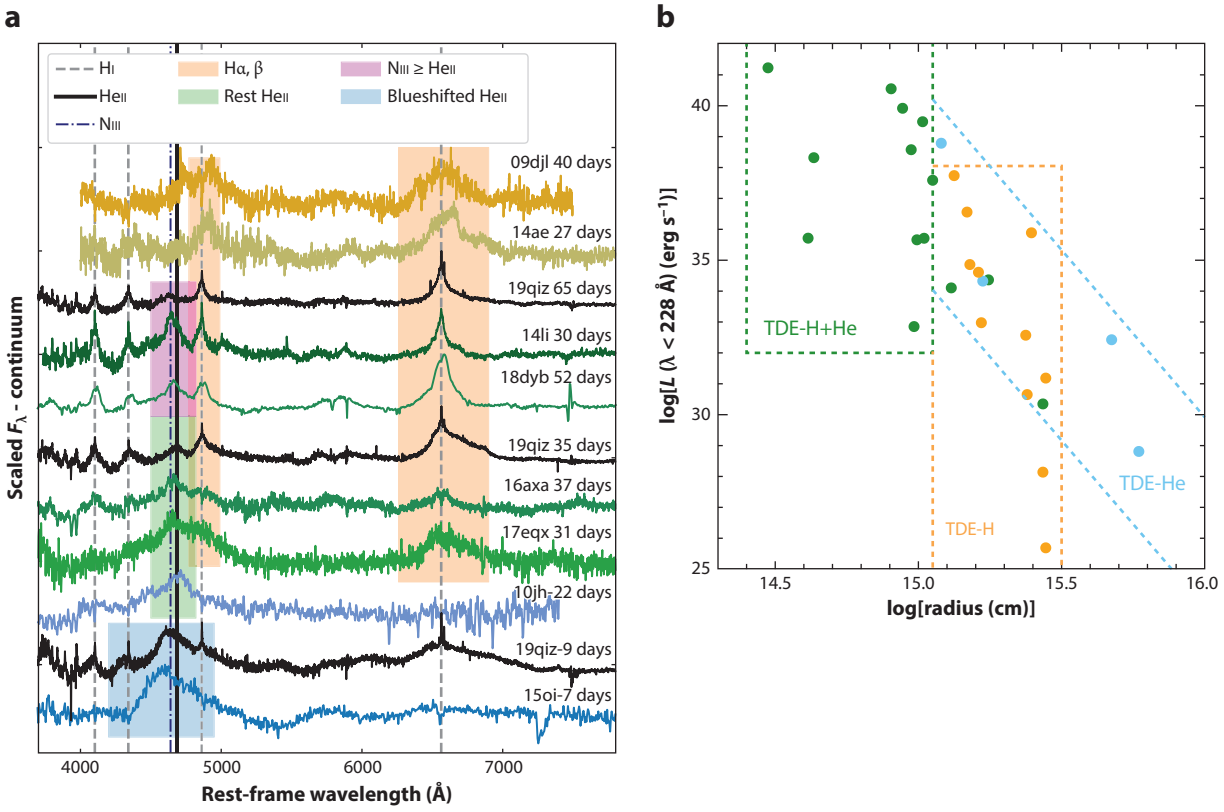

Figure 5

(*a*) Spectroscopic classes of TDEs labeled by their phase in days since peak and highlighted by the presence of broad HeII λ4686 (TDE-He); the presence of broad He, Hα, and Hβ (TDE-H+He); the presence of strong Bowen fluorescence feature NIII λ4640; and those with only broad H features (TDE-H). Panel adapted from Nicholl et al. (2020) with permission. (*b*) Plot of the blackbody luminosity below 228 Å capable of ionizing He and triggering the Bowen fluorescence mechanism, based on the temperature and bolometric luminosity of the UV-optical component, versus the inferred radius of the UV-optical photosphere. Points are color-coded by their spectral class. Note that the TDE-H+He-class objects appear to prefer more UV luminous flares with more compact radii than the TDE-H class. TDE-He class objects appear in a larger range of radii and luminosities.

prefer higher EUV luminosities and compact radii compared to the TDE-H class, whereas the TDE-He class show a range of conditions. Another important clue is the relative rates of the spectral types. Note that among the 17 TDEs in the Year 1.5 ZTF TDE sample, only one was He only! Given that the host-galaxy properties and flare properties do not stand out for this one object, AT2018iih/ATLAS18yzs, it may be indicating that it was the disrupted star's properties that were unique (i.e., He rich). However, a simple picture connecting spectral class with TDE parameters is complicated further by the detection of a TDE by Pan-STARRS, AT2017eqx/PS17dhz, that transitioned over a timescale of 100 days from being H dominated to He dominated, with the HeII line blueshifted by 5,000 km s^{-1} (Nicholl et al. 2019). Nicholl et al. (2019) explain this spectral transformation as being due to a contracting atmosphere, eventually revealing a wind in the polar direction. The contracting atmosphere is needed to suppress H emission at late times, which is expected in the Roth et al. (2016) model for optically thick atmospheres with a certain radius.

Wevers et al. (2019) noted the emergence of FeII lines in AT2018fyk/ASASSN-18ul and ASASSN-15oi, signaling the presence of low-ionization lines from optically thick, dense gas.

Furthermore, they argued that because the FeII complex is visible during a secondary maximum in the UV-optical light curve of AT2018fyk/ASASSN-18ul, perhaps both the low-ionization lines and the UV-optical plateau are a result of reprocessing of the soft X-ray radiation into the UV-optical wavebands.

3.4. Line Profiles

The profiles of TDE emission lines are very broad [(3–13) $\times$ 10^4 km s^{-1}; Arcavi et al. 2014, Hung et al. 2017, Holoien et al. 2019a], and in some cases with double-peaked, boxy, and/or blue-shifted structures. Such large velocities are expected in a TDE. If one assumes that the lines are broadened by Doppler broadening of the gas in the gravitational potential of the central black hole, then one can translate the velocity width of the line to a radius in gravitational radii, $v \approx c(2r_g/r)^{1/2}$(Brown et al. 2017). Specifically, the velocity at the tidal radius is expected to be $v \approx 43{,}700 M_6^{1/3} \frac{\rho_\star}{\rho_\odot}^{1/6}$ km s^{-1}, where $\rho_\star$ is the average density of the disrupted star (Arcavi et al. 2014). The unbound tidal debris streams have a lower characteristic velocity, with the most energetic bound material being ejected at speeds of $v \approx 7{,}500 M_6^{1/6} m_\star^{1/3} r_\star^{-1/2}$ km s^{-1} (Strubbe & Quataert 2009), and should have a narrow profile due to the small velocity dispersion in the tidal tail of unbound debris (Bogdanović et al. 2004).

PTF-09dj (Arcavi et al. 2014) was the first TDE to be fitted by a double-peaked profile to its very broad Hα line, albeit the circular Keplerian disk model fit required an extra redshift of 15,000 km s^{-1} to match the wavelengths of the red and blue peaks, and a better fit was achieved, without a bulk redshift, with an elliptical disk (having a large disk inclination), and a pericenter orientation nearly vertical to the observer (Liu et al. 2017). Furthermore, Cao et al. (2018) argue that even single-peaked broad line profiles in TDEs can be fitted using extremely eccentric disk models with a pericenter position nearly pointing toward the observer and a low disk inclination.

The double-peaked profile of the Hα line in PS18kh was modeled by Holoien et al. (2019a) with an elliptical disk with an eccentricity of $e = 0.25$. However, Hung et al. (2019) favored an expanding spherical outflow model with a flat-topped shape to fit the line profile, because of the identification of narrow absorption features in the broad Hα line that were mimicking a double-peaked profile. The most extreme case for a double-peaked line profile is that observed in the Balmer lines of AT2018hyz/ASASSN-18zj, which are well fitted with a circular disk model in some epochs but with evolution in the line profile that requires an additional variable Gaussian broad-line component (Hung et al. 2020, Short et al. 2020). The flat Balmer decrement observed in this source (Hα/Hβ $\sim$ 1.5) was also argued to be the signature of collisional excitation of the line emission, possibly in the chromosphere of the disk.

One model prediction is that in the presence of an optically thick wind, the lines should be broadened due to electron scattering out of the photosphere (Roth & Kasen 2018). Indeed, an observed trend for the broad TDE lines is that they decrease in line width with time. Holoien et al. (2016b) noted that this is opposed to what is expected from reverberation of a fading continuum. In an AGN, the line width is determined by the kinematics of the broad-line gas. Thus, as the continuum fades, you would expect broader lines due to the decreasing radius, and thus higher gas velocities, for which the virialized gas around the black hole was photoionized. If instead line width is set by electron scattering, then the evolution of the line width depends on the evolution of the optical depth of the scattering medium. In the unified TDE model presented by Dai et al. (2018), due to the wind launched by the super-Eddington accreting debris disk, the optical depth to electron scattering is viewing angle dependent, increasing from the poles to the plane of the disk. Disentangling these effects is critical for using the line shapes to extract the geometry and kinematics of the photoionized gas.

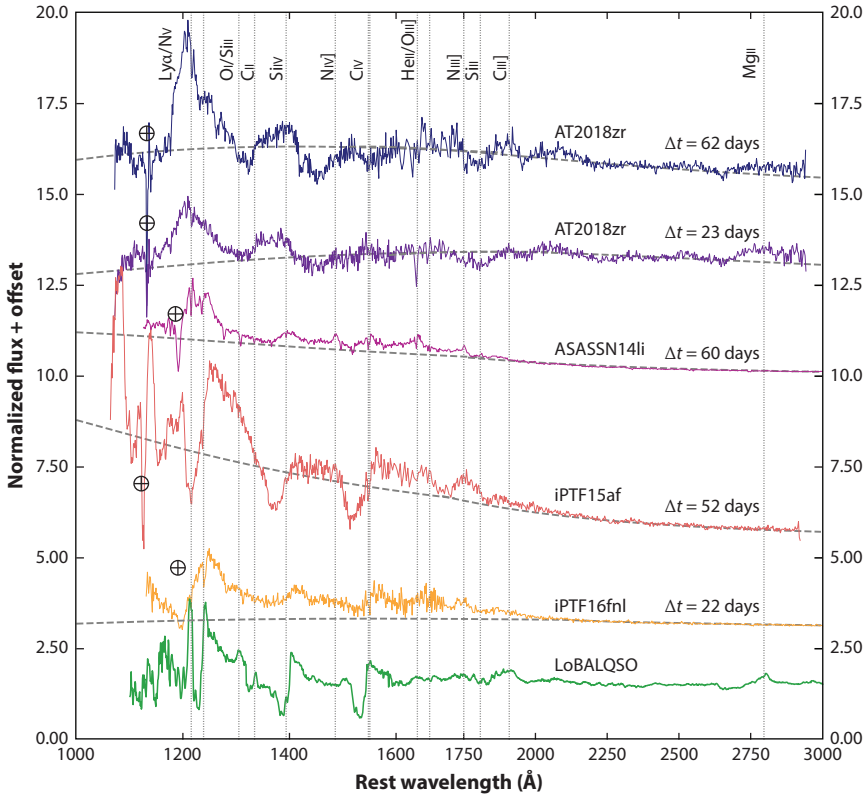

Figure 6

HST/STIS UV spectroscopy of TDEs. Broad absorption and emission UV-resonance lines are detected on top of a hot, blue continuum, including Lyα, Nv λ 1240, Siiv λ 1400, and Civ λ 1550. A UV spectrum of a LoBALQSO is shown for comparison. Figure adapted from Hung et al. (2019) with permission.
Abbreviation: LoBALQSO, low-ionization broad absorption line quasar.

3.5. UV Spectroscopy

UV spectroscopy is a precious resource, because it requires observations from space to evade absorption from Earth's atmosphere. The HST/STIS instrument has played an important role in revealing the spectroscopic properties of TDEs in the UV. As of now, there are only four TDEs with UV spectra (**Figure 6**): ASASSN-14li (Cenko et al. 2016), iPTF-16fnl (Brown et al. 2018), iPTF-15af (Blagorodnova et al. 2019), and AT2018zr/PS18kh (Hung et al. 2019). They are characterized by a hot continuum and strong, broad UV-resonance lines, in emission and sometimes absorption, including Lyα, Nv λ1240, Siiv λ1400, and Civ λ1550. They have many spectral features in common with BALQSOs but are notable for the higher strength of nitrogen features relative to carbon, and the relative weakness of C III] λ1909, and Mg II λ2796, 2804, similar to the rare class of N-rich QSOs.

Interestingly, Yang et al. (2017) argue that given that C and N are colocated in the same photoionization zone, their ratio is not as sensitive to photoionization conditions (density of the gas or shape of the photoionizing continuum) as it is to their relative chemical abundances. The measured abundance ratios measured for nitrogen to carbon from UV lines of C III] λ1908/N III] λ1750 indicate N-enriched material. Indeed, Kochanek (2016) argues that the disrupted star's mass and

evolutionary state on the main sequence will be imprinted on the TDE spectrum, including the enhancement of He, and the rapid enhancement of N and the depletion of C in the CNO cycle for stars more massive than 1 $M_\odot$.

Recently, Parkinson et al. (2020) came up with a unification scheme for TDE UV spectra using a Monte Carlo ionization and radiative transfer code, in which the lines are produced in a biconical accretion disk wind, broad absorption lines are produced for sight lines into the wind cone, and broad emission lines are produced otherwise. This model successfully reproduces the diversity of UV spectra shown in **Figure 6**, including the suppression of CIV λ1550 relative to NV λ1240 due to CNO-processed chemical abundances of the stellar debris.

3.6. Infrared Dust Echoes

In the presence of dust, the UV-bright flare of a TDE is absorbed and reemits in the MIR, producing a luminous echo (Lu et al. 2016). Indeed, archival searches of WISE data revealed luminous, delayed MIR flares from three TDEs, including ASASSN-14li (Jiang et al. 2016, van Velzen et al. 2016), PS16dtm (Jiang et al. 2017), and OGLE17aaj (Yang et al. 2019). In a study of quiescent galaxies with variable MIR emission measured by WISE, there were 14 candidates for long-term fading that could be attributed to a TDE (Wang et al. 2018). The detection of increased FeII emission in several of the TDEs with dust echoes was explained by Fe released into the gas phase from dust grains by UV photons, providing direct evidence for dust sublimation by the TDE flare (Jiang et al. 2019).

One of the advantages of detecting a dust echo is that the luminosity in the MIR can be used as a bolometer, to determine the total luminosity emitted by the TDE, even without direct access to the unobservable portions of the SED, such as the EUV, where the bulk of the TDE emission is expected to be emitted. Van Velzen et al. (2016) show that from the estimation of the dust reprocessing shell, R, assuming it has the size of the sublimation radius, it will have a radius of

$$R_{\rm dust} \approx 0.15 \left(\frac{L_{45}}{a_{0.1}^2 T_{1850}^{5.8}} \right)^{1/2} \text{pc}, \qquad 7.$$

where $L_{45} = L/10^{45}$ erg s^{-1} is the luminosity of the flare; $a_{0.1} = a/0.1\,\mu$m, where a is the size of the dust grains; and $T_{1850} = T_{\rm dust}/1{,}850$ K. Thus from measuring the dust temperature from the MIR colors, and inferring the radius from the time delay of the dust echo with respect with the TDE flare, where $\tau \sim R_{\rm dust}/c$ (Jiang et al. 2016), one can infer the peak luminosity over all frequencies in which dust absorbs radiation from the TDE. Then the covering factor of the dust can be determined from the ratio of the total energy radiated by the dust in the MIR by the energy absorbed by the dust, $f_{\rm dust} = E_{\rm dust}/E_{\rm abs}$. One interesting trend is that $f_{\rm dust}$ appears to be quite low for TDEs, ∼1% (van Velzen et al. 2016). This is much smaller than the covering fraction inferred from MIR flares from changing-look AGN (CLAGN). CLAGN are AGN that transform in spectral type, broad-line (Type 1) to narrow-line (Type 2), and vice versa, accompanied by a luminous flare of continuum radiation. CLAGN are expected to have a preexisting dusty torus, and thus their characteristic higher values of $f_{\rm dust}$ could be a potential discriminator between TDEs and CLAGN for the source of the flaring continuum radiation (Frederick et al. 2019).

3.7. Coronal Line Emitters

Another manifestation of a TDE is line emission powered by gas in the vicinity of the black hole that is photoionized by the flare of radiation from the TDE. The class of extreme coronal line emitters (ECLEs), galaxies with transient, fading narrow line emission of [Fe VII], and coronal

lines from [Fe X] to [Fe XIV], and in some cases broad recombination lines of Hα, Hβ, and HeII λ4686, have been argued to be the result of photoionization by a TDE (Komossa et al. 2008, Wang et al. 2012, Yang et al. 2013). Dou et al. (2016) also found fading MIR emission associated with these coronal line emitter TDE candidates, providing further evidence that these were powered by TDEs in a gas-rich environment. In fact, Palaversa et al. (2016) were able to recover the nuclear flare that powered the high-ionization lines in one of the ECLEs from archival LINEAR (Lincoln Near-Earth Asteroid Research Asteroid Survey) optical monitoring data, as well as follow-up *Swift* observations of archival GALEX UV detection, which confirmed the fading of the UV emission after the flare. In general, ECLEs allow us to probe the effects of TDEs on much longer timescales than the accretion event itself, thanks to light travel time delays as the flare propagates through a gas-rich circumnuclear medium (Wang et al. 2012). Future, massively multiplexed fiber spectrographic surveys could yield a large population of ECLEs and place a valuable, independent constraint on the TDE rate.

3.8. X-Rays

There are now 11 UV-optically selected TDEs that have been detected in the soft X-rays: GALEX D3-13, GALEX D1-9, ASASSN-14li, ASASSN-15oi, AT2018zr/PS18kh, AT2018hyz/ASASSN-18zj, AT2019azh/ASASSN-19dj, AT2019dst/ZTF19aapreis, AT2019ehz/Gaia19bpt, AT2018fyk/ASASSN-18ul, and OGLE16aaa. Although the spectral properties of the soft X-ray component in these TDEs share the same characteristics of the soft X-ray-selected TDEs—an extremely soft spectrum well fitted by blackbody temperatures that range from 0.02–0.13 keV (see **Figure 2**)—the relative brightness of this component compared with the UV-optical component can range from 1 to 10^3 (Gezari et al. 2017; Wevers et al. 2019; van Velzen et al. 2019, 2021), and shows dramatic variability with time, which is unlike the smoothly evolving power-law decline of the UV-optical flare, and is often completely uncorrelated. Understanding what is driving the wide range and variability of the optical to X-ray ratio in TDEs may be the most revealing diagnostic for what is powering these two components: accretion, reprocessing, or stream–stream collisions.

In the cases of ASASSN-15oi (Gezari et al. 2017, Holoien et al. 2018) and AT2019azh/ASASSN-19dj (Liu et al. 2019, van Velzen et al. 2021), there was a gradual brightening in the soft X-rays over a timescale of a year in which the UV-optical component was declining from peak. In the case of AT2018fyk/ASASSN-18ul, the TDE is detected in the soft X-rays at early times, but with a factor of 2–5 variability on the timescale of days, and then shows brightening at late times, but then shows a dramatic brightening by a factor of 10 in just 6 days, which is 3 months after the peak of the flare, resulting in a rapid decrease in the optical-to-X-ray ratio (Wevers et al. 2019). OGLE16aaa (Kajava et al. 2020) showed the rapid appearance of soft X-rays 6 months after the optical peak, followed by a decline to a lower, steady-state soft X-ray flux over the next year.

In order to characterize the relative strength of the UV-optical and soft X-ray components, I use the commonly used definition of α_{ox} for characterizing the SEDs of AGNs, but modify it to measure the ratio of the monochromatic luminosity density at 2500 Å to 0.5 keV, instead of 2 keV, because most of the TDEs show such soft spectra that they are not detected above 1 keV. I use the unabsorbed X-ray luminosity density corrected for the Galactic HI column density, and the UV luminosity for the Galactic extinction. Thus, I define

$$\alpha_{osx} = \frac{\log[L_\nu(2500\ \text{Å})/L_\nu(0.5\ \text{keV})]}{\log[\nu(2500\ \text{Å})/\nu(0.5\ \text{keV})]} = 0.5\log[L_\nu(0.5\ \text{keV})/L_\nu(2500\ \text{Å})]. \quad 8.$$

In the case in which $\nu L_\nu(0.5\ \text{keV}) = \nu L_\nu(2500\ \text{Å})$, one gets $\alpha_{osx} = -1$. In AGNs, there is an anticorrelation between α_{ox} and $L_\nu(2500\ \text{Å})$ (Maoz 2007), although in this case α_{ox} is measured

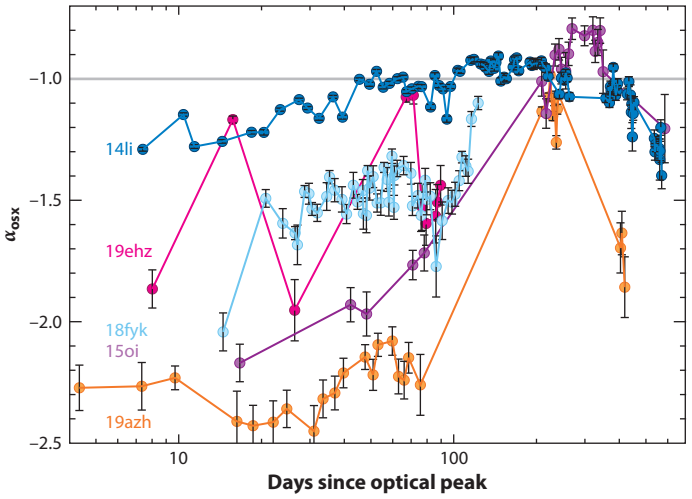

Figure 7

Dramatic X-ray variability of TDEs detected with both a UV-optical and soft X-ray component, characterized with the parameter α_{osx}, and measured from *Swift*/XRT and *Swift*/UVOT *uvw2* observations of ASASSN-14li, ASASSN-15oi, AT2018fyk/ASASSN-18ul, AT2019azh/ASASSN-19dj, and AT2019ehz/Gaia19bt. Gray line shows the characteristic value of $\alpha_{osx} = -1$, which corresponds to $\nu L_\nu(2500\ \text{Å})/\nu L_\nu(0.5\ \text{keV}) = 1$.

at 2 keV and is a comparison of the relative strength of UV emission from the big blue bump associated with thermal emission from the accretion disk and nonthermal hard X-ray emission associated with the AGN corona. It can be seen in the 5 TDEs with well-sampled UV and soft X-ray light curves from *Swift* follow-up observations in **Figure 7** that there is strong variability in α_{osx} of the TDEs, with a general trend of increasing α_{osx} with time, suggestively peaking near $\alpha_{osx} = -1$. In the case of AT2019ehz/Gaia19bpt, the soft X-ray flux appears to flare by a factor >10 on timescales of just a few days, with $\alpha_{osx} \sim -1$ during each flare (van Velzen et al. 2021). In the cases of ASASSN-15oi and AT2019azh/ASASSN-19dj, the soft X-ray flux increases by a factor >10 over 200 days, with α_{osx} increasing from −2.2 to −1.0, but with no evidence of a change in absorbing column density and no significant evolution in temperature (Gezari et al. 2017, Hinkle et al. 2021a). AT2018fyk/ASASSN-18ul showed variability of a factor of 2–5 on the timescale of days, and then, 100 days after peak, brightens by a factor of 10 in less than a week (Wevers et al. 2019), approaching close to $\alpha_{osx} \sim -1$, but again with no evidence of a change in line-of-sight absorption.

Understanding what is driving this variability on both short (∼day) and long (∼year) timescales is critical for determining if variable obscuration and/or delayed accretion is determining the optical to soft X-ray flux ratio. Already, the lack of an obvious decrease in line-of-sight column density with increasing soft X-ray luminosity is problematic for the obscuration scenario. However, it may be that if the opacity is dominated by electron scattering by a highly ionized medium (Dai et al. 2018), then the soft X-rays can be obscured without changing the observed spectral slope as is the case for absorption by neutral gas.

3.9. Evidence for Jets and Outflows

One of the biggest surprises in TDE observations was the discovery of a class of relativistic TDEs, whose luminous, nonthermal radiation was explained as viewing a jet face on that was launched

by a TDE. In retrospect, this class of TDE is a natural extension of the blazar class for AGNs, and the impact of jets on the radiation from TDEs had already been discussed in the literature in the context of jets interacting with the circumnuclear medium. The detection of such radio emission was not actualized until the discovery of the low-redshift optically selected TDE ASASSN-14li. For the first time, a multiwavelength campaign was able to detect several components of emission from this TDE across the electromagnetic spectrum, including transient radio emission.

The radio emission from ASASSN-14li was interpreted as synchrotron emission from either external shocks—driven by the interaction of a nonrelativistic outflow (Alexander et al. 2016), the unbound debris streams (Krolik et al. 2016), or a relativistic jet (van Velzen et al. 2016) with the circumnuclear medium—or internal shocks in a relativistic jet (Pasham & van Velzen 2018). However, the detection of a correlation between the X-ray and radio light curves, with $L_{\rm radio} \propto L_{\rm X}^2$, suggests that the accretion and jet power are linearly coupled (Pasham & van Velzen 2018). This follows from the fact that the synchrotron luminosity from a power-law distribution of electrons with index p in the radio scales with the jet power (Q_j) as $L_{\rm radio} \propto Q_j^{1+\frac{p+1}{4}}$. Thus, for $p = 3$ and $L_{\rm radio} \propto L_{\rm X}^2$, where $L_X \propto \dot{M}_{\rm acc}$, one gets $Q_j \propto \dot{M}_{\rm acc}$. Pasham & van Velzen (2018) also observe a time lag between soft X-ray and radio wavelengths of 12 days, which is self-consistent with their model for a freely expanding canonical jet. The strong coupling between the accretion rate and jet power strongly favor the internal jet model over an external emission mechanism (Pasham & van Velzen 2018, Bright et al. 2018).

Radio emission has also been detected from XMMSL1 J0740-85 (Alexander et al. 2017) and AT2019dsg (Stein et al. 2020), suggesting that radio follow-up observations, or even radio-blind searches for transient radio emission (Anderson et al. 2020), can place important constraints on the nature and frequency of jets and outflows in TDEs. Already one can infer from radio follow-up that high radio-luminosity, relativistic jets similar to Swift J1644+57 must occur in only 1% of TDEs (Alexander et al. 2020).

The super-Eddington accretion rates in TDEs make them especially conducive to launching an outflow. This outflow could manifest itself as bright optical emission from the reprocessing of higher-energy emission from the accretion disk (Strubbe & Quataert 2009, Lodato & Rossi 2011, Metzger & Stone 2016) or in the form of absorption lines, particularly in the UV Strubbe & Quataert (2011). Highly ionized outflows have now been detected from spectra in the X-rays from ASASSN-14li (Miller 2015, Kara et al. 2018), and in the UV from ASASSN-14li (Cenko et al. 2016), iPTF16fnl (Brown et al. 2018), iPTF15af (Blagorodnova et al. 2019), and AT2018zr/PS18kh (Hung et al. 2019), with a wide range of velocities, sometimes blue-shifted and sometimes red-shifted, reflecting a diverse set of physical conditions in the outflow in terms of their geometry, kinematics, and optical depth (Hung et al. 2019). Progress in mapping the UV spectra of TDEs to the geometry and orientation of the accretion disk wind is critical for testing models in which the optical-to-X-ray ratio is determined by the inclination angle to a radiatively driven wind (Dai et al. 2018). In general, understanding the radiation, winds, and jets from TDE accretion disks provides important insight to the feedback mechanisms of AGNs in general.

4. TENSIONS BETWEEN OBSERVATIONS AND TDE THEORY

4.1. Large Inferred Radii

One of the common properties of both X-ray and UV-optically selected TDEs is the thermal nature of their continuum. This is expected for the continuum from the circularized, accreting debris disk. Following the classical relations for an optically thick, geometrically thin accretion

disk, one expects a peak effective temperature of (Miller 2015)

$$T_{\rm eff,peak} = 0.54 \left(\frac{\dot{M}}{\dot{M}_{\rm Edd}} \frac{G^2 M_{\rm BH}^2}{\kappa \sigma \eta c R_{\rm in}^3} \right)^{1/4} \approx 4 \times 10^5 \, {\rm K} \left(\frac{\dot{M}}{\dot{M}_{\rm Edd}} \right) (\eta/0.1)^{-1/4} M_{\rm BH}^{-1/4}, \qquad 9.$$

where κ is the opacity due to electron scattering. Both components are well described by a blackbody, albeit with a factor of ~10 difference in temperature. The first TDE candidates, discovered in the soft X-rays by the ROSAT survey, initially were puzzling owing to their relatively small inferred radii, using the simple relation for a blackbody, $L = 4\pi\sigma R_{\rm BB} T^4$, which is even smaller than the Schwarzschild radius of the central black hole. However, the next generation of TDE candidates, discovered in UV and optical surveys, had the opposite problem. Their inferred radii were too large compared to the expectations of the size of the circularized debris disk, with $R_{\rm disk} = 2R_{\rm T}$. These disagreements with the basic theoretical predictions of accretion-powered emission from a circularized debris disk has necessitated the development of more complex theories, involving a reprocessing envelope (Loeb & Ulmer 1997, Guillochon et al. 2014), electron scattering (Li et al. 2002), stream-stream collisions (Piran et al. 2015, Jiang et al. 2016), and radiatively driven winds (Metzger & Stone 2016).

In **Figure 8**, I show the radius of the observed blackbody emission in 49 out of the 56 TDEs in **Table 1** with a black hole mass inferred from the host-galaxy mass measured from the

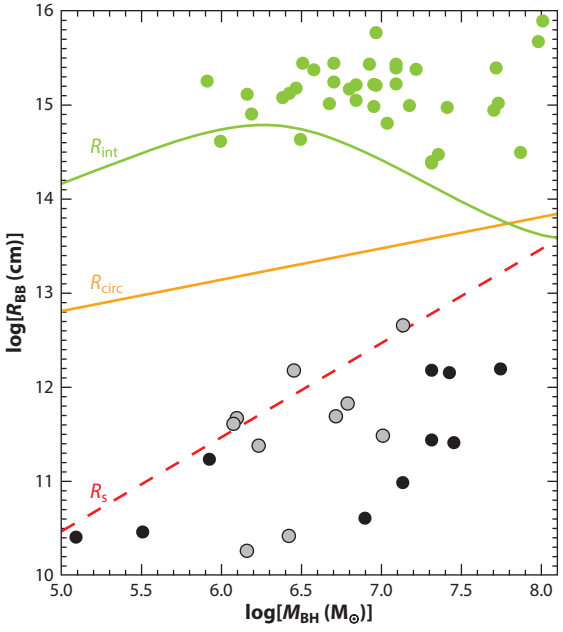

Figure 8

Blackbody radius as a function of black hole mass estimated from the total galaxy mass for UV-optically selected TDEs (*green*), X-ray-selected TDEs (*black*), and the soft X-ray component of UV-optically selected TDEs (*gray*). Although the radius of the soft X-ray component appears to track the increase of the Schwarzschild radius linearly with mass ($R_{\rm S} \propto M_{\rm BH}$; plotted with a *red dashed line*), the UV-optical component appears not to have a strong dependence on black hole mass, is a factor of 100 larger than the expected size of the circularized debris disk, $R_{\rm circ} \sim 2R_{\rm T}$ (plotted in *yellow*), and is more consistent with the self-intersection radius of the debris streams (plotted in *green* for an impact parameter $\beta = 1$), and it also has a weak dependence on $M_{\rm BH}$.

broadband SED for 10 of the X-ray TDE hosts (Graur et al. 2018, Wevers et al. 2019, French et al. 2020) and 39 of the UV-optical TDE hosts (van Velzen 2018, van Velzen et al. 2021), to estimate $M_{\rm BH}$. I use the correlation between the total galaxy mass ($M_{\rm gal}$) and $M_{\rm BH}$ measured from dynamical masses of early and late-type galaxies from Greene et al. (2020), $\log(M_{\rm BH}/{\rm M}_\odot) = 7.56 + 1.39[\log(M_{\rm gal}/{\rm M}_\odot) - 10.48]$, with an intrinsic scatter of 0.79 dex. This relation is most relevant for estimating $M_{\rm BH}$ for the TDE hosts because it is based on the total galaxy mass and, thus, does not require knowledge of the bulge-to-total ratio, which is not well measured for most of the host galaxies. However, the relation is based on only five galaxies below $10^{10}\,{\rm M}_\odot$ with dynamical black hole masses, and there appear to be two different normalizations between the early-type and late-type galaxies. The $M_{\rm BH}$ versus $\sigma_\star$ relation has a smaller scatter (0.53 dex) and does not have this difference in normalization between the galaxy types. Thus, continued high spectral resolution follow-up of TDE galaxy hosts is critical for the best constraints on $M_{\rm BH}$.

Figure 8 also shows the expectations for the various characteristic size scales for a TDE as a function of $M_{\rm BH}$, including $R_{\rm S} = 2GM_{\rm BH}/c^2$, and

$$R_{\rm circ} = (1 + e_0)R_{\rm p} \sim 2R_{\rm T} \qquad 10.$$

circularization radius due to angular momentum conservation, where e_0 is the initial eccentricity and $R_{\rm p}$ is the pericenter of the star's orbit.

$$R_{\rm I} = \frac{a_{\rm mb}(1 - e_{\rm mb}^2)}{[1 - e_{\rm mb}\cos(\phi/2)]}, \qquad 11.$$

the self-intersection radius from Dai et al. (2015), where $e_{\rm mb} \approx 1 - (2/\beta)(\frac{M_\star}{M_{\rm BH}})^{1/3}$ is the eccentricity of the orbit of the most bound debris, $\phi = \frac{6\pi GM_{\rm BH}}{a_{\rm mb}(1-e_{\rm mb}^2)c^2}$ is the angle of apsidal precession, and $a_{\rm mb} = R_{\rm T}^2/(2R_\star)$ is the semimajor axis of the most bound debris (Dai et al. 2015, Bonnerot et al. 2016).

The characteristic radii of the UV-optical thermal component in TDEs are much larger than expected for a debris disk formed from the circularized debris streams, and the soft X-ray thermal component in TDEs is often even smaller than the size of the event horizon of the black hole ($R_{\rm S}$). Both situations are problematic, and require an expansion of the simplest TDE models. Interestingly, the UV-optical component is close to the size of the self-intersection radius of the debris streams, as pointed out by Wevers et al. (2019). An important consideration is also whether the UV-optical component is powered by reprocessing of the soft X-ray component or is in fact a source of emission generated from the shock interaction of the debris streams themselves. In the following section, we examine the relative behavior of these two components in order to determine their origin.

4.2. Large Optical to X-Ray Ratio, and Its Evolution with Time

Two of the most intriguing questions in TDE observations include why are many optically selected TDEs faint in the X-rays and what is driving the X-ray variability observed in several optically selected TDEs? The main explanation for the high optical-to-X-ray ratio in TDEs has been either (*a*) obscuration or (*b*) delayed accretion. In the case of an optically thick wind, the material is initially opaque to X-rays due to electron scattering. It is not until the ejecta expands and becomes completely ionized by the inner disk radiation after $t_{\rm ion} \approx 2t_{\rm fb}\beta^{-3.4}M_6^{-1.1}m_\star^{0.71}$ that the soft X-rays can escape (Metzger & Stone 2016), implying that for the largest black holes, $t_{\rm ion} \ll t_{\rm fb}$, and the X-ray radiation escapes promptly, resulting in an X-ray luminous TDE. However, viewing angle effects may come into play if the geometry of the accretion flow allows for some lines of sight out of the wind and directly toward the inner accretion disk (Dai et al. 2018).

Another nice outcome of this model is that the radiation diffused through the wind results in an effective temperature of

$$T_{\rm eff} = \left(\frac{L_{\rm rad}}{4\pi\sigma R_{\rm wind}^2}\right)^{1/4} \approx 2.1\times10^4\,{\rm K}(\eta/0.1)^{1/4}\beta^{-1/4}m_\star^{13/60}M_6^{-13/24}\left(\frac{t}{t_{\rm fb}}\right)^{-11/12} \quad 12.$$

and provides a potential explanation for the observed temperature of the UV-optical component in TDEs, but not their relatively constant temperature with time. Several TDEs show an increase in temperature with time (van Velzen et al. 2021, Hinkle et al. 2020), challenging these models even further. However, this model's prediction for a cooling of the temperature with time does not account for the fact that as the material expands, and becomes optically thin, the photosphere will recede to deeper layers, resulting in a slower evolution of $T_{\rm eff}$.

However, there are more complications. This model assumes that the material circularizes and forms an accretion disk with $t_{\rm circ} \ll t_{\rm fb}$. In fact, this process depends sensitively on the central black hole mass. In several numerical and analytical studies, most recently by Bonnerot & Lu (2020), it is the smaller-mass black holes for which the circularization timescale is quite long (Bonnerot et al. 2016),

$$t_{\rm circ} = 8.3t_{\rm fb}M_6^{-5/3}\beta^{-3} \quad 13.$$

and this was dubbed "A Dark Year for Tidal Disruptions" by Guillochon & Ramirez-Ruiz (2015). The smaller black holes also result in stream–stream collisions further from the black hole, resulting in longer viscous timescales, because the debris that accretes onto the black hole from that self-intersection point is subject to the viscous timescale at that distance:

$$t_{\rm visc} = \alpha^{-1}(h/r)^{-2}P_{\rm circ}, \quad 14.$$

where $P_{\rm circ} = 2\pi\sqrt{a_{\rm circ}^3/GM_{\rm BH}}$. If $t_{\rm fb} \ll t_{\rm visc}$, then the accretion rate will be slowed with respect to the fallback rate, also resulting in a reduced peak luminosity.

An alternative model to explaining the weak X-ray luminosity at early times in optically selected TDEs is that the optical emission is powered locally by shock heating from stream-stream collisions near apocenter, which thermalizes and diffuses out through the infalling matter with an intrinsic temperature of

$$T \sim 3.3\times10^4 m_\star^{1/10}M_6^{-3/8}\,{\rm K}, \quad 15.$$

thereby matching the observed temperature of the UV-optical component in TDEs without requiring the reprocessing of soft X-radiation from an accretion flow. In this model, the UV-optical emission and the soft X-ray emission are completely decoupled, and one could explain the late-time brightening of the soft X-ray emission in some TDEs as delayed accretion in a circularizing debris disk. There already is some evidence for a black hole mass dependence on the emergence of a late-time UV plateau in optically selected TDEs, explained as delayed emission from a viscously spreading accretion disk in the TDEs with lower-mass black holes ($M_{\rm BH} < 10^{6.5}\,{\rm M}_\odot$) (van Velzen et al. 2019). This result is important in that it also implies that the prompt UV-optical component of these TDEs is not powered by accretion!

4.3. Correlations (or Lack Thereof) with Central Black Hole Mass

One of the robust predictions of TDE theory is that there should be a maximum central black hole mass, above which a star will cross the event horizon before being disrupted, i.e., $R_{\rm T} > R_{\rm S}$, which occurs for

$$M_{\rm BH} < \frac{c^3}{M_\star^{1/2}}\left(\frac{R_\star}{2G}\right)^{3/2} = 1.1\times10^8\,{\rm M}_\odot m_\star^{-1/2}r_\star^{3/2}, \quad 16.$$

where $r_\star = R_\star/\mathrm{R}_\odot$ and $m_\star = M_\star/\mathrm{M}_\odot$. Van Velzen (2018) showed that indeed the luminosity function of TDEs as a function of black hole mass (measured from the host-galaxy bulge velocity dispersion) did show an intrinsic cutoff at $\sim 10^8\,\mathrm{M}_\odot$ and argued this was clear evidence for the black hole event horizon. The one exception to this cutoff was ASASSN-15lh, a TDE candidate [also argued to be a SLSN by Dong et al. (2016)] from the center of a passive red galaxy with an inferred central black hole mass (from the host-galaxy stellar mass) of $\sim 6 \times 10^8\,\mathrm{M}_\odot$, which is well above the Hills mass of a nonrotating (Schwarzschild) black hole for a solar-type star. However, a star could be disrupted outside the event horizon for this black hole mass if it was either a maximally spinning (Kerr) black hole or the star was massive ($M_\star > \mathrm{M}_\odot$). However, given the old stellar population of the host galaxy measured from stellar population synthesis fits to its SED, a spinning black hole was favored (Leloudas et al. 2016).

Furthermore, given that the tidal disruption radius, fallback timescale, and peak mass accretion rate have dependencies on black hole mass, one would expect the properties of the TDE flares to correlate with M_{BH}. Currently, the most stringent constraints on M_{BH} for TDE hosts come from stellar velocity dispersion measurements. Wevers et al. (2019) reported black hole mass estimates for 23 TDE hosts using homogeneous measurements of the flux-weighted central stellar velocity dispersion ($\sigma_\star$) from medium-resolution ($\Delta v \sim 15$–$60\ \mathrm{km\ s^{-1}}$), optical long-slit spectra and found a relatively flat distribution of M_{BH} in the range of $5 < \log(M_{\mathrm{BH}}/\mathrm{M}_\odot) < 8$, with no significant difference in black hole masses between the optically selected and X-ray-selected TDEs.

However, the ultimate goal for TDE observations is to use the properties of the TDE itself to weigh the mass of the central black hole, instead of relying on indirect host-galaxy scaling relations. Indeed, Mockler et al. (2019) attempted to do so by fitting multiband optical light curves with a model based on numerical simulations of the fallback rate ($\dot{M}_{\mathrm{fb}}$) as a function of stellar polytropic index (γ) and impact parameter (β), and fitting for an accretion efficiency (η), where $\dot{M}_{\mathrm{fb}} = L/(\eta c^2)$, and adjusting η such that the luminosity cannot exceed the Eddington limit. In order to fit the temperatures and constant colors characteristic of optically selected TDEs, the model includes the addition of a reprocessing photosphere with a radius that can change with a power-law dependence on the luminosity and with a minimum and maximum radius set by the innermost stable circular orbit of the black hole (R_{isco}) and the semimajor axis of the debris streams (a_0), respectively. Finally, the model also allows for a viscous delay to account for potential delays between the fallback of material and its subsequent accretion via an accretion disk. This parametric model, fitted with a Markov chain Monte Carlo routine to find the highest-likelihood model parameters with Bayesian statistics (`MOSFiT`), yields a constraint on M_{BH} and $M_\star$ (Mockler et al. 2019). However, the black hole masses derived from `MOSFiT` show just a marginal agreement with the black hole masses inferred from the host-galaxies' properties. This is not surprising, because it is not clear yet that the observable parameters of a TDE, such as rise time or peak luminosity, even scale with M_{BH} as expected for a light curve powered solely by fallback accretion.

We now have 22 TDEs with prepeak sampling of their light curves: PS1-10jh (Gezari et al. 2012), PS1-11af (Chornock et al. 2014), PTF09ge (Arcavi et al. 2014), iPTF16fnl (Blagorodnova et al. 2017), and 15 out of the 17 TDEs in ZTF (van Velzen et al. 2021), plus AT2018dyb/ASASSN-18pg (Leloudas et al. 2019), AT2018fyk/ASASSN-18ul (Wevers et al. 2019), and AT2019ahk/ASASSN-19bt (Holoien et al. 2019b) (see **Figure 4** for some examples). This enables us to investigate how their rise time to peak correlates with other TDE parameters and host-galaxy properties. In **Figure 9**, I plot the e-folding rise timescale to the peak luminosity, $\Delta t_{e,\,\mathrm{rise}}$, and e-folding decay timescale, $\Delta t_{e,\,\mathrm{decay}}$, as measured by van Velzen et al. (2020), as a function of inferred black hole mass from the host-galaxy mass. As found by van Velzen et al. (2021), there is a correlation between luminosity and rise time, but surprisingly there is no correlation between rise time and inferred central black hole mass. Interestingly, if the rise time was tracing

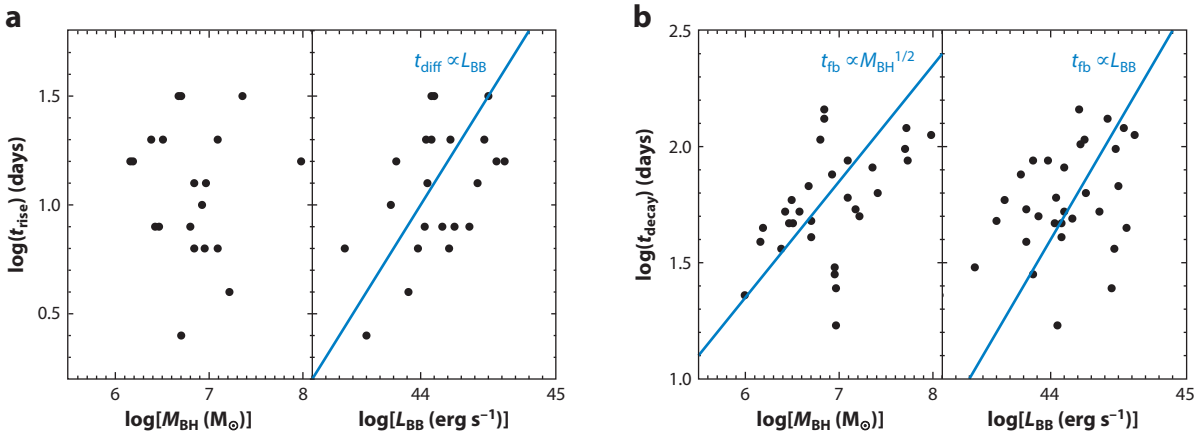

Figure 9

(*a*) Correlation (or lack thereof) of rise timescale with black hole mass and peak luminosity for TDEs with black hole mass estimates from their total galaxy mass, and a well-sampled prepeak light curve. Correlations for the fallback rate shown in blue. (*b*) Correlation of decay timescale with black hole mass and peak luminosity for TDEs with black hole mass estimates from their total galaxy mass. Correlations for the fallback rate shown in blue.

the fallback timescale, then because $t_{fb} \propto M_{BH}^{1/2}$ and $L_{peak} \propto M_{BH}^{-1/2}$, one would expect $t_{peak} \propto L_{peak}^{-1}$. If instead, the rise time is tracing the radiative diffusion timescale, $t_{diff} \propto \rho R^2$, which for a spherical distribution of radius R and mass M translates to $t_{diff} \propto M/R$, then if the radius of the photosphere is set by the intersection radius of the debris streams, R_{int}, and the peak luminosity traces the mass accreted, one gets $t_{diff} \propto L/R_{int}$, and then one would get the positive correlation between L and t_{rise} that is observed. With a similar argument, van Velzen et al. (2021) explained that the lack of the expected correlation of $t_{peak} \propto M_{BH}^{-1/2}$ could be attributed to photon trapping in the presence of an outflow, which will prolong the rise time to peak if $t_{tr} > t_{fb}$, where $t_{tr}/t_{fb} \propto M_{BH}^{-1/2}$ (Metzger & Stone 2016), and thus should be a more important effect for less-massive black holes.

It has been proposed that, instead of using fits to the TDE light curve, one can simply use the observed temperature and UV-optical luminosity at peak to infer M_{BH} and $M_\star$, if the UV-optical emission is powered by the dissipation of energy by shocks intersecting near the apocenter of the highly eccentric orbits of the stellar debris, where

$$a_0 = \frac{GM_{BH}}{\Delta\epsilon} = M_{BH}^{2/3} R_\star M_\star^{-2/3} \propto M_{BH}^{2/3} M_\star^{2/9}, \qquad 17.$$

and assuming a mass–radius relation of $R_\star \propto M_\star^{8/9}$ (Ryu et al. 2020a). Because the luminosity from the shock in this model scales as $L_{sh} \sim \frac{GM_{BH}\dot{M}}{a_0} \propto M_{BH}^{-1/6} M_\star^{4/9}$, and the temperature scales as $T \propto [\frac{L_{sh}}{\sigma \Delta\Omega a_0^2}]^{1/4}$, then one gets $T \propto M_{BH}^{-3/8}$ (Ryu et al. 2020a). Interestingly, this method does provide black hole mass estimates that are in good agreement with the black hole mass estimated from the host-galaxy bulge mass, which is another piece of evidence in favor of the physical model in which stream–stream shocks at $r \sim a_0$ are powering the UV-optical component, instead of reprocessing emission from a more compact, circularized accretion disk with $r \sim R_T$.

Another intriguing signal to probe M_{BH}, which originates from the heart of the accreting black hole in a TDE, is quasi-periodic emission from the innermost stable circular orbit (R_{isco}) around the black hole. Quasi-periodic oscillations have been reported in two TDEs, in an analysis of the nonthermal hard X-ray light curve of jetted TDE Swift J1644+57 (Reis et al. 2012) ($P = 200$ s), and of the soft thermal X-ray light curve of optically selected TDE ASASSN-14li (Pasham et al.

2019) ($P = 131$ s). This period corresponds to a radius of $R = (\frac{GM_{\rm BH}P^2}{4\pi^2})^{1/3} \sim 0.1(\frac{P}{[100{\rm sec}]})^{2/3} M_6 R_{\rm S}$, and with a knowledge of the spin parameter, a, and assuming the emission originates from $R_{\rm ISCO}$, because $R_{\rm isco} = 3R_{\rm S}$ for $a = 0$ to $R_{\rm isco} = R_{\rm S}/2$ for a maximally spinning ($a = 0.998$) black hole, it can be used to determine $M_{\rm BH}$.

4.4. Observed Rates: Too Low, Too High, or Just Right?

The expected rate of TDEs in galaxy nuclei has been both analytically and numerically determined from calculations of stellar orbits for galaxies of various stellar density profiles (core versus cusp) as well as black holes of different configurations (Schwarzschild, Kerr, binary, recoiling). One of the most exciting applications of measuring the TDE rate as a function of galaxy type and black hole mass is distinguishing between these scenarios. For example, measuring the TDE rate on the low-mass end can shed light on the black hole occupation fraction in low-mass galaxies, which is a potential discriminator between black hole seed formation models (Stone & Metzger 2016). Measuring the TDE rate on the high-mass end can probe the spin distribution of MBHs (Kesden 2012a). However, though the TDE event rate is well determined, predictions for the observed tidal disruption flare rate relies on several assumptions: the peak luminosity, effective temperature, and galaxy central black hole mass. One can take an empirical approach and start with the observed luminosities, temperatures, and light curves. However, there may be a population of TDEs that the current survey selection techniques are missing or an error in our assumptions about the black hole mass function that is poorly constrained in low-mass galaxies. Comparing the theoretical rate with the observational rate can thus be quite revealing.

Measuring the TDE rate ($\dot{N}$) per galaxy requires an understanding of each survey's detection efficiency, $\epsilon \equiv N^{-1} \sum_i^N \epsilon_i$, where ϵ_i is the detection efficiency for each TDE detection, effective survey time (τ), and number of galaxies monitored ($N_{\rm gal}$), where $\dot{N} = (N_{\rm TDE}/N_{\rm gal})\tau\epsilon$ (van Velzen & Farrar 2014). In order to calculate ϵ, one must make assumptions about the luminosity and time evolution of TDEs. The first attempts to measure $\dot{N}$ from X-ray and optical survey data resulted in rates of $\sim 10^{-5}$ year^{-1} galaxy^{-1} (Donley et al. 2002, Esquej et al. 2008, Gezari et al. 2009, van Velzen & Farrar 2014, Holoien et al. 2016b), which is an order of magnitude below the expectations from dynamical models, but were based on the detection of only 2–3 TDEs in each survey.

This tension with the theoretical expectation of the rate from loss-cone dynamics using realistic stellar density profiles of 10^{-4} year^{-1} galaxy^{-1} (Magorrian & Tremaine 1999, Wang & Merritt 2004) was initially attributed to selection effects due to insensitivity to faint and fast, or long-timescale, TDEs (Kochanek 2016); conservative candidate filtering for SNe or AGNs; our uncertainty in the nature of the optical emission component, which may not be present in all TDEs; or an anisotropic velocity distribution of stellar orbits, with a bias toward tangential velocities that would suppress the TDE rate from two-body relaxation (Stone & Metzger 2016).

However, with larger samples of TDEs now available, the observed TDE rates appear to be coming into agreement with theoretical expectations. If one is interested in the volumetric rate ($\dot{n}$), one needs to take into account not the number of galaxies but the total volume surveyed. Using the $1/\mathbf{V}_{\rm max}$ method, where $\mathbf{V}_{\rm max} \equiv V(z_{\rm max})A \times \tau$, and A is the area of the survey, $z_{\rm max}$ is the maximum redshift that one could detect a TDE of a given luminosity by the flux limit of the survey, and $V(z_{\rm max})$ is the corresponding volume per unit area. Using the value of $\sum 1/\mathbf{V}_{\rm max}$ in bins of luminosity, van Velzen (2018) derived a luminosity function of TDEs from 17 TDEs from the literature, well fitted with a steep power law of the form

$$\frac{{\rm d}\dot{N}}{{\rm d}\log_{10} L} = \dot{N}_0 (L/L_0)^a, \qquad 18.$$

where $L_0 = 10^{43}$ erg s^{-1}, $\dot{N}_0 \sim 2 \times 10^{-7}$ Mpc^{-3} year^{-1}, and $a \sim -1.5$. One can then make a more accurate estimate of the TDE rate per galaxy, by calculating ϵ using the observed luminosity function instead of a constant characteristic luminosity or a model-dependent luminosity. Indeed, van Velzen (2018) finds a per galaxy rate of 1×10^{-4} year^{-1} galaxy^{-1} by using the observed host-galaxy stellar mass function from the $1/\mathbf{V}_{\max}$ method, now coming into agreement with theoretical predictions. Similarly, Hung et al. (2017) derived a TDE rate from the systematic follow-up of iPTF nuclear transients in the UV with *Swift*, resulting in two TDE detections, and assuming the steep luminosity function from van Velzen (2018) dominated by less luminous flares, resulting in a rate of $\sim 1.7 \pm 10^{-4}$ year^{-1} galaxy^{-1}. A recent update to the van Velzen (2018) calculation by van Velzen et al. (2020), with double the sample of TDEs from adding the most recent influx of optical TDE discoveries in the literature, yields a slightly lower overall rate of 6×10^{-5} year^{-1} galaxy^{-1}.

One of the challenges for the next generation of surveys is how to filter transients down to TDE candidates without making assumptions about their properties that would bias the survey against finding the full population of TDEs. However, despite these challenges we are finding that the observed TDE rate is in general agreement with dynamical predictions and with important preferences in the host-galaxy types.

4.5. Do TDEs Prefer Post-Starburst Galaxy Hosts? If So, Why?

Given that the TDE rate should be primarily driven by stellar dynamics within the sphere of influence of the central black hole, the rates and properties of TDEs should correlate with host-galaxy stellar density and structure. It was surprising, however, when Arcavi et al. (2014) noted that several TDEs were hosted in a rare subclass of galaxies with no active star formation and a bright population of A stars resulting in strong Hδ absorption known as E+A galaxies. This was broadened further by French et al. (2016) to be a preference for quiescent, Balmer strong galaxies, which are more common than E+A galaxies, that make up only $\sim$2% of the local galaxy population, which was 75% of the optical TDE hosts known at the time. This puzzling overrepresentation of TDEs in this rare galaxy type was attributed to several effects, including a recent galaxy merger (potentially yielding a binary MBH with an enhanced TDE rate,) or a higher concentration of A stars susceptible for disruption.

However, TDE hosts also share other properties, including in colors predominantly in the green valley of the mass–color diagram (Law-Smith et al. 2017, Hammerstein et al. 2021, van Velzen et al. 2021) and high central stellar density (Law-Smith et al. 2017, Graur et al. 2018, Hammerstein et al. 2021), both favorable conditions for stellar disruptions. Using forward modeling techniques, Roth et al. (2020) find that they can explain the lack of ZTF TDE hosts in the blue locus of galaxies in the mass–color diagram from dust obscuration in star-forming galaxies. However, selection effects alone cannot explain the overrepresentation of E+A galaxy hosts. However, Hammerstein et al. (2021) note that the overrepresentation of the quiescent, Balmer strong, E+A (H$\delta > 4$ Å) galaxies disappears to $\mathcal{O}(1)$ when selecting from only the green and centrally concentrated galaxy population.

5. FUTURE PROSPECTS

5.1. Improving Search Strategies from the Ground and in Space

Although survey capabilities in the optical band have been steadily increasing, and will have a large jump in survey power with the beginning of the Vera Rubin Observatory Legacy Survey of Space and Time (LSST) in just a couple years, our selection strategies for discovering TDEs will

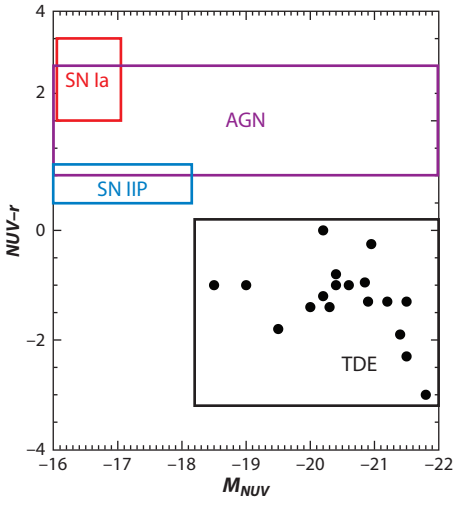

Figure 10

Classification power of UV imaging to disentangle optical transients associated with AGNs and SNe from bona fide TDEs, from their extremely blue UV-optical colors and high UV luminosities at peak. Abbreviations: AGNs, active galactic nuclei; SNe, supernovae.

still be hampered by intensive filtering of more common interlopers, such as AGNs and SNe. One feature of TDEs that has been critical for their confirmation from optical candidates has been their uniform property of bright, persistent UV emission. In **Figure 10**, I show the UV-optical color versus their absolute magnitude in the *NUV* of TDEs, measured by *Swift* follow-up of optically selected TDEs, in comparison to the mean UV properties at the optical peak of SNe Ia measured by *Swift* (Milne et al. 2013), and by the GALEX satellite for Type II-P SNe (Gezari et al. 2015) and AGNs (Gezari et al. 2013).

It is striking how easily the UV-optical color alone can be used to filter our SNe. With a wide-field, UV space telescope, observing concurrently with ground-based optical surveys, one could promptly distinguish TDEs from SNe, and clear the fog of contaminants, without the labor of follow-up spectroscopy and the potential incompleteness introduced by filtering down the full transient alert stream.

There is still a possibility that searching for TDEs with the UV-optical properties of the optically selected TDE candidates may miss an entire population of TDEs that are not UV-bright! Although X-ray follow-up has been possible for the promptly discovered optical TDEs, there has been much less comprehensive multiwavelength follow-up for the soft X-ray-selected TDEs. It may be that the component producing the UV-optical component, whether from stream–stream collisions, reprocessing, or a combination of both, is not present in all TDE systems. A soft X-ray-selected TDE sample, with contemporaneous optical monitoring, could address the following important questions:

- Are optical and X-ray-selected TDEs tracing the same population?
- What are the parameters that favor optical versus X-ray emission?
- How does the optical and X-ray evolution of the TDEs constrain emission models?
- What are the timescales for the formation of an accretion disk in a TDE as a function of its black hole mass?
- What is the true TDE rate?

With new X-ray survey capabilities, such as the extended Roentgen Survey with an Imaging Telescope Array (eROSITA) on board the Russian-German Spektrum-Roentgen-Gamma (SRG) mission, currently conducting an all-sky X-ray (0.5–2 keV) survey, there soon should be a much larger sample (potentially thousands) of X-ray-selected TDEs to shed light on these questions (Khabibullin et al. 2014).

An exciting X-ray signal that is predicted, but has yet to be detected, for stars on deep encounters at the moment of pericenter passage is a shock break out when the shock produced from the tidal compression of the star propagates through and heats the deformed star (Carter & Luminet 1983, Brassart & Luminet 2008), resulting in a pulse of X-ray radiation, with a temperature of $k_{\rm B}T \sim \frac{GM_\star m_{\rm p}}{R_\star} \sim 1\, m_\star r_\star^{-1}$ keV, a duration on the order of the crossing time, $\delta t \sim R_\star/v_{\rm p} \sim 10\, m_\star^{-1/6} r_\star^{3/2} M_6^{-1/3}$ s, where $v_{\rm p} \sim c(R_{\rm g}/R_{\rm T})^{1/2}$ is the orbital velocity at periastron, and a luminosity of $L_{\rm X} \lesssim 10^{42}\, m_\star^{19/12} r_\star^{-5/4} M_6^{1/6}$ ergs s^{-1} (Kobayashi et al. 2004, Yalinewich et al. 2019). The detection of shock breakout would provide a clean time stamp for the time of disruption. Detecting this brief X-ray burst is challenging, however, and requires a combination of wide area and high sensitivity in the X-ray band, potentially achievable with future X-ray telescopes being developed with lobster-eye X-ray optics (Hudec et al. 2017).

5.2. Intermediate-Mass Black Holes

One of the most exciting prospects of using TDEs as probes of MBH demographics is using the detection of the disruption of a white dwarf (WD) as a smoking-gun signature of an IMBH, the elusive missing link between MBHs and stellar-mass black holes from the remnants of the evolution of massive stars [see the recent review on IMBHs by Greene et al. (2020)]. The reason for this is that given the high density of a WD, and the fact that the maximum mass for which a star is disrupted outside the event horizon scales as $M_{\rm max} \propto R_\star^{3/2}/M_\star^{1/2} \propto \rho_\star^{1/2}$, WDs can only be disrupted by lower-mass black holes. Assuming typical values of a CO white dwarf of $M_{\rm WD} \sim 0.6\,{\rm M}_\odot$ and $R_{\rm WD} \sim 0.014{\rm R}_\odot$, one gets $M_{\rm max} \sim 2 \times 10^5\,{\rm M}_\odot$. Furthermore, given the distinct radii and compositions of CO WDs from He WDs, formed from the truncated evolution of red giants in a close binary system, one could use the observed TDE spectra to distinguish between them (Law-Smith et al. 2017) and get a more accurate measurement of $M_{\rm BH}$ from the timescales of the system.

Indeed, there is at least one candidate for a WD disruption by an IMBH from the detection of [OIII]λ5007 and [NII]λ6583 narrow line emission, and no detection of H Balmer emission lines, from a globular cluster in the Fornax elliptical galaxy, NGC 1399, which is also coincident with an ultraluminous X-ray source (Irwin et al. 2010). The strong oxygen line, and the lack of any H Balmer line emission, was interpreted as emission from photoionized H-free gas from a tidally disrupted star around an IMBH powering the X-ray emission via accretion, although the strong [NIII] emission is not predicted from photoionization models for the spectrum from a disrupted CO white dwarf (Clausen & Eracleous 2011). Unfortunately, there is no optical spectral information about the other IMBH candidate TDE detected by *Chandra* from a dwarf galaxy (Maksym et al. 2013), which would definitively identify it as a WD disruption and, thus, require an IMBH.

In general, a WD TDE will be a challenge to detect, because the characteristic timescales for a WD disruption are very short, $t_{\rm fb} \sim 2\,{\rm min}\,(0.014/{\rm R}_\odot)^{3/2} M_5^{1/2} (0.6/{\rm M}_\odot)^{-1}$, and the peak luminosities are lower, due to the lower Eddington luminosity of the IMBH involved. However, another potential manifestation of a WD disruption is the detonation of thermonuclear runaway from the tidal compression of the WD in a deep encounter with the IMBH, resulting in an SN-like transient powered by the radioactive decay of iron-group elements from explosive nuclear burning (Brassart & Luminet 2008, Rosswog et al. 2009, Anninos et al. 2018). This would result in a Type

Ia SN-like thermonuclear transient, albeit likely underluminous in comparison, due to the much different geometry and lower ejecta mass involved in the explosion (MacLeod et al. 2016).

5.3. TDEs as Multimessenger Sources

TDEs are also promising as multimessenger sources, providing the exciting opportunity to combine signals from light, gravitational waves, and/or neutrinos to produce a vivid physical picture of the strong gravity and particle acceleration in these events. As multimessenger detector capabilities continue to advance, the potential for TDEs as multimessenger probes of massive black holes will become increasingly important.

5.3.1. Very high-energy neutrinos. The first multimessenger observation of a TDE is the IceCube South Pole Neutrino Observatory detection of a very high-energy neutrino in the direction of a radio- and X-ray-detected optical TDE discovered by ZTF, AT2019dsg/ZTF19aapreis (Stein et al. 2020), establishing TDEs as a potential site for PeV (petaelectronvolt) neutrino production. The detected ∼0.2-PeV neutrino must have been produced by protons accelerated to high energies (>4 PeV) that then collided with a photon target ($p\gamma$ production) from the thermal TDE continuum or a proton target (pp production), in the form of the unbound stellar debris or the radio-emitting $v \sim 0.1c$ outflow. No gamma-ray emission was detected by the *Fermi Large Area Telescope*. However, a coincident TeV (teraelectronvolt) gamma-ray signal, potentially detectable with gamma-ray Cherenkov telescopes, would confirm a hadronic origin, because the pp production produces a power-law neutrino spectrum, which would be accompanied by lower-energy gamma rays. Future multimessenger observations of TDEs in PeV neutrinos, TeV neutrinos, and gamma rays can distinguish between these neutrino production mechanisms and be used to model the contribution of TDEs to the diffuse cosmic neutrino flux.

5.3.2. Gravitational waves. With the detection of the neutron star binary merger GW170817 in gravitational waves and in light across the electromagnetic spectrum, we officially entered a new era of multimessenger astronomy (Abbott et al. 2017). From this one source, one learned how combining information from gravitational waves (GWs) and light can reveal profound insights into the physical properties of a transient like never before. Because the GW strain for a binary system scales as

$$h \sim \frac{GM_\star R_\mathrm{g}}{c^2 D R_\mathrm{p}} \sim 2 \times 10^{-22} \beta \left(\frac{D}{10\,\mathrm{Mpc}}\right)^{-1} r_\star^{-1} m_\star^{4/3} M_6^{2/3}, \qquad 19.$$

with a frequency of

$$f \sim \left(\frac{GM_\mathrm{BH}}{R_\mathrm{p}^3}\right)^{1/2} \sim 6 \times 10^{-4} \beta^{3/2} m_\star^{1/2} r_\star^{-3/2}\,\mathrm{Hz}, \qquad 20.$$

the best chance of detecting a TDE in GWs is from the tidal disruption of a compact star, like a WD, on a deep encounter with a black hole, with a low-frequency GW detector like the *Laser Interferometer Space Antenna* (LISA), but out to a distance of only 10 kpc (Kobayashi et al. 2004, Rosswog et al. 2009, Anninos et al. 2018). This again favors the tidal disruption around an IMBH and is therefore an even more exciting probe for IMBHs speculated to exist in dwarf galaxy nuclei and/or globular clusters (Greene et al. 2020). With both a GW and electromagnetic signal, one could use the chirp mass measured from the GW signal, as well as the exact timing of the pericenter passage of the star, together with the light generated from the debris streams to model the accretion flow in detail, and determine the true timescale for circularization and accretion (Eracleous et al. 2019). However, even without producing a detectable GW signal themselves,

TDEs can provide a useful constraint on the rate of detecting GWs from extreme-mass-ratio inspirals of compact objects into MBHs that will be an important signal for LISA.

6. CONCLUSIONS

In this review, I have highlighted the exciting progress in the discovery of TDEs from wide-field X-ray, UV, and optical surveys, including the buildup of a statistically significant sample of TDEs with well-sampled light curves and detailed multiwavelength characterization of their emission from the radio to the hard X-rays. The panchromatic emission detected from TDEs probe a wide range of scales, from the innermost regions of a newly forming accreting debris disk to the first collisions of debris streams as they fall back on the black hole after disruption, to the expansion of the unbound debris, wind, or jet into the circumnuclear medium, and the heating of circumnuclear dust. Although TDEs are now well established as a class of nuclear transients with common, distinguishable properties, there are still important unknowns about what powers their luminous emission. However, they certainly have realized their potential as probes of accretion onto $6 < \log(M_{\rm BH}/{\rm M}_\odot) < 8$ black holes, and may be the only observable probes of accretion onto IMBHs [$\log(M_{\rm BH}/{\rm M}_\odot) < 5$] in the future.

The most important observed trends can be summarized as follows:

- The power-law decline rate of TDE light curves follows the expectation for emission that follows the fallback rate, $t_{\rm fb} \propto M_{\rm BH}^{1/2}$, but the rise time does not; rather, the rise time is more closely related to the radiative diffusion timescale.
- The characteristic radius of the UV-optical thermal emission in TDEs is consistent with the spatial scale of the intersection radius of the bound debris streams near apocenter, whereas the characteristic radius of the soft X-ray component is consistent with $R_{\rm isco}$ or even smaller.
- TDEs can be grouped into three spectral classes, TDE-H, TDE-H+He, and TDE-He, with the TDE-H+He class showing Bowen fluorescence line emission and a preference for a hotter and more compact line-emitting region. The TDE-He class is the rarest and may be associated with the tidal disruption of evolved or stripped stars with He-rich composition.
- The spectral line profiles of TDEs in the optical and UV are very broad and, with detailed photoionization modeling, can be good tracers of the kinematics and geometry of the stellar debris disk and its associated wind.
- The UV to soft X-ray ratio in TDEs is highly variable and appears to approach a ratio close to unity at late times. However, the lack of a decrease in observed line-of-sight absorption with increasing soft X-ray flux disfavors the unveiling of the soft X-ray emission through an expanding reprocessing layer.
- IR echoes and transient coronal line emission are valuable indirect probes of TDEs from their influence on their gas and dust in the circumnuclear environment.
- There is strong evidence for outflows and/or jets powered by TDEs from the UV, radio, and X-ray wavelengths. Mapping their properties as a function of TDE parameters can provide insight into jet formation and AGN feedback.
- Observational constraints on the rate of TDEs are improving and appear to be consistent with the expectations of stellar dynamical models.
- TDEs have a strong preference for galaxies in the green valley with centrally concentrated stellar density profiles, which may be the underlying cause for their frequent detection in E+A galaxy hosts.
- The future is bright for multiwavelength and multimessenger observations of TDEs, and their use as probes of central MBH demographics, accretion physics, and jet formation over cosmic time.

DISCLOSURE STATEMENT

The author is not aware of any affiliations, memberships, funding, or financial holdings that might be perceived as affecting the objectivity of this review.

ACKNOWLEDGMENTS

I want to thank my close collaborators in the observational hunt for TDEs from the Zwicky Transient Facility "black hole" Science Working Group, especially Sjoert van Velzen, S. Brad Cenko, Matthew Graham, and Shri Kulkarni, and my terrific team of current and former graduate students, who have spent many nights observing, and days scanning for, TDEs: Tiara Hung, Sara Frederick, Charlotte Ward, and Erica Hammerstein. I acknowledge support for some of this work from the National Science Foundation CAREER grant 1454816, and from several NASA *Neil Gehrels Swift* and XMM-*Newton* grants. I also want to thank the Aspen Center for Physics, supported by National Science Foundation grant PHY-1607611, for hosting our 2018 Winter Workshop on "Using Tidal Disruption Events to Study Super-Massive Black Holes," which was one of the first conferences dedicated to TDEs. Finally, I want to thank my "village," Tanikwa, Gloria, Lexi, Natalie, my husband Chase, and The Sherwood Forest Boys and Girls Camp, without whose wonderful care of my adorable children, Cutter, Steele, Brooke, and Ryder, I would not have been able to focus on finishing my review during a global pandemic.

LITERATURE CITED

Abbott BP, Abbott R, Abbott TD, Acernese F, Ackley K, et al. 2017. *Ap. J. Lett.* 848:L12
Alexander KD, Berger E, Guillochon J, Zauderer BA, Williams PKG. 2016. *Ap. J. Lett.* 819:L25
Alexander KD, van Velzen S, Horesh A, Zauderer BA. 2020. *Space Sci. Rev.* 216:81
Alexander KD, Wieringa MH, Berger E, Saxton RD, Komossa S. 2017. *Ap. J.* 837:153
Anderson MM, Mooley KP, Hallinan G, Dong D, Phinney ES, et al. 2020. *Ap. J.* 903:116
Anninos P, Fragile PC, Olivier SS, Hoffman R, Mishra B, Camarda K. 2018. *Ap. J.* 865:3
Arcavi I, Gal-Yam A, Sullivan M, Pan YC, Cenko SB, et al. 2014. *Ap. J.* 793:38
Bade N, Komossa S, Dahlem M. 1996. *Astron. Astrophys.* 309:L35–38
Bellm EC, Kulkarni SR, Graham MJ, Dekany R, Smith RM, et al. 2019. *Publ. Astron. Soc. Pac.* 131:018002
Beloborodov AM, Illarionov AF, Ivanov PB, Polnarev AG. 1992. *MNRAS* 259:209–17
Blagorodnova N, Cenko SB, Kulkarni SR, Arcavi I, Bloom JS, et al. 2019. *Ap. J.* 873:92
Blagorodnova N, Gezari S, Hung T, Kulkarni SR, Cenko SB, et al. 2017. *Ap. J.* 844:46
Blagorodnova N, Neill JD, Walters R, Kulkarni SR, Fremling C, et al. 2018. *Publ. Astron. Soc. Pac.* 130:035003
Blanchard PK, Nicholl M, Berger E, Guillochon J, Margutti R, et al. 2017. *Ap. J.* 843:106
Bloom JS, Giannios D, Metzger BD, Cenko SB, Perley DA, et al. 2011. *Science* 333:203
Bogdanović T, Cheng RM, Amaro-Seoane P. 2014. *Ap. J.* 788:99
Bogdanović T, Eracleous M, Mahadevan S, Sigurdsson S, Laguna P. 2004. *Ap. J.* 610:707–21
Bonnerot C, Lu W. 2020. *MNRAS* 495:1374–91
Bonnerot C, Rossi EM, Lodato G, Price DJ. 2016. *MNRAS* 455:2253–66
Bowen IS. 1935. *Ap. J.* 81:1
Bower GC. 2011. *Ap. J. Lett.* 732:L12
Bower GC, Metzger BD, Cenko SB, Silverman JM, Bloom JS. 2013. *Ap. J.* 763:84
Brassart M, Luminet JP. 2008. *Astron. Astrophys.* 481:259–77
Bright JS, Fender RP, Motta SE, Mooley K, Perrott YC, et al. 2018. *MNRAS* 475:4011–19
Brockamp M, Baumgardt H, Kroupa P. 2011. *MNRAS* 418:1308–24
Brown GC, Levan AJ, Stanway ER, Tanvir NR, Cenko SB, et al. 2015. *MNRAS* 452:4297–306
Brown JS, Holoien TWS, Auchettl K, Stanek KZ, Kochanek CS, et al. 2017. *MNRAS* 466:4904–16
Brown JS, Kochanek CS, Holoien TWS, Stanek KZ, Auchettl K, et al. 2018. *MNRAS* 473:1130–44
Brown JS, Stanek KZ, Holoien TWS, Kochanek CS, Shappee BJ, et al. 2019. *MNRAS* 484:3785–96

Cao R, Liu FK, Zhou ZQ, Komossa S, Ho LC. 2018. *MNRAS* 480:2929–38
Cappellari M, Renzini A, Greggio L, di Serego Alighieri S, Buson LM, et al. 1999. *Ap. J.* 519:117–33
Cappelluti N, Ajello M, Rebusco P, Komossa S, Bongiorno A, et al. 2009. *Astron. Astrophys.* 495:L9–12
Carter B, Luminet JP. 1983. *Astron. Astrophys.* 121:97–113
Cenko SB, Bloom JS, Kulkarni SR, Strubbe LE, Miller AA, et al. 2012a. *MNRAS* 420:2684–99
Cenko SB, Cucchiara A, Roth N, Veilleux S, Prochaska JX, et al. 2016. *Ap. J. Lett.* 818:L32
Cenko SB, Krimm HA, Horesh A, Rau A, Frail DA, et al. 2012b. *Ap. J.* 753:77
Chambers KC, Magnier EA, Metcalfe N, Flewelling HA, Huber ME, et al. 2016. arXiv:1612.05560
Chan CH, Piran T, Krolik JH, Saban D. 2019. *Ap. J.* 881:113
Chornock R, Berger E, Gezari S, Zauderer BA, Rest A, et al. 2014. *Ap. J.* 780:44
Clausen D, Eracleous M. 2011. *Ap. J.* 726:34
Coughlin ER, Nixon CJ. 2019. *Ap. J. Lett.* 883:L17
Dai L, McKinney JC, Miller MC. 2015. *Ap. J. Lett.* 812:L39
Dai L, McKinney JC, Roth N, Ramirez-Ruiz E, Miller MC. 2018. *Ap. J. Lett.* 859:L20
Donato D, Cenko SB, Covino S, Troja E, Pursimo T, et al. 2014. *Ap. J.* 781:59
Dong S, Shappee BJ, Prieto JL, Jha SW, Stanek KZ, et al. 2016. *Science* 351:257–60
Donley JL, Brandt WN, Eracleous M, Boller T. 2002. *Astron. J.* 124:1308–21
Dou L, Wang TG, Jiang N, Yang C, Lyu J, Zhou H. 2016. *Ap. J.* 832:188
Eracleous M, Gezari S, Sesana A, Bogdanovic T, MacLeod M, et al. 2019. *Bull. Am. Astron. Soc.* 51:10
Esquej P, Saxton RD, Freyberg MJ, Read AM, Altieri B, et al. 2007. *Astron. Astrophys.* 462:L49–L52
Esquej P, Saxton RD, Komossa S, Read AM, Freyberg MJ, et al. 2008. *Astron. Astrophys.* 489:543–54
Evans CR, Kochanek CS. 1989. *Ap. J. Lett.* 346:L13
Frank J, Rees MJ. 1976. *MNRAS* 176:633–47
Frederick S, Gezari S, Graham MJ, Cenko SB, van Velzen S, et al. 2019. *Ap. J.* 883:31
French KD, Arcavi I, Zabludoff A. 2016. *Ap. J. Lett.* 818:L21
French KD, Wevers T, Law-Smith J, Graur O, Zabludoff AI. 2020. *Space Sci. Rev.* 216:32
Gafton E, Rosswog S. 2019. *MNRAS* 487:4790–808
Gezari S, Basa S, Martin DC, Bazin G, Forster K, et al. 2008. *Ap. J.* 676:944–69
Gezari S, Cenko SB, Arcavi I. 2017. *Ap. J. Lett.* 851:L47
Gezari S, Chornock R, Rest A, Huber ME, Forster K, et al. 2012. *Nature* 485:217–20
Gezari S, Heckman T, Cenko SB, Eracleous M, Forster K, et al. 2009. *Ap. J.* 698:1367–79
Gezari S, Jones DO, Sanders NE, Soderberg AM, Hung T, et al. 2015. *Ap. J.* 804:28
Gezari S, Martin DC, Forster K, Neill JD, Huber M, et al. 2013. *Ap. J.* 766:60
Gezari S, Martin DC, Milliard B, Basa S, Halpern JP, et al. 2006. *Ap. J. Lett.* 653:L25–28
Giannios D, Metzger BD. 2011. *MNRAS* 416:2102–7
Golightly ECA, Coughlin ER, Nixon CJ. 2019a. *Ap. J.* 872:163
Golightly ECA, Nixon CJ, Coughlin ER. 2019b. *Ap. J. Lett.* 882:L26
Gomez S, Nicholl M, Short P, Margutti R, Alexander KD, et al. 2020. *MNRAS* 497:1925–34
Graur O, French KD, Zahid HJ, Guillochon J, Mandel KS, et al. 2018. *Ap. J.* 853:39
Greene JE. 2012. *Nat. Commun.* 3:1304
Greene JE, Strader J, Ho LC. 2020. *Annu. Rev. Astron. Astrophys.* 58:257–312
Greiner J, Schwarz R, Zharikov S, Orio M. 2000. *Astron. Astrophys.* 362:L25–28
Grupe D, Thomas HC, Leighly KM. 1999. *Astron. Astrophys.* 350:L31–34
Guillochon J, Manukian H, Ramirez-Ruiz E. 2014. *Ap. J.* 783:23
Guillochon J, Ramirez-Ruiz E. 2013. *Ap. J.* 767:25
Guillochon J, Ramirez-Ruiz E. 2015. *Ap. J.* 809:166
Halpern JP, Gezari S, Komossa S. 2004. *Ap. J.* 604:572–78
Hammerstein E, Gezari S, van Velzen S, Cenko SB, Roth N, et al. 2021. *Ap. J. Lett*. 908:L20
Hills JG. 1975. *Nature* 254:295–98
Hinkle JT, Holoien TWS, Auchettl K, Shappee BJ, Neustadt JMM, et al. 2021. *MNRAS* 500:1673–96
Hinkle JT, Holoien TWS, Shappee BJ, Auchettl K, Kochanek CS, et al. 2020. *Ap. J. Lett.* 894:L10
Holoien TWS, Auchettl K, Tucker MA, Shappee BJ, Patel SG, et al. 2020. *Ap. J.* 898:161

Holoien TWS, Brown JS, Auchettl K, Kochanek CS, Prieto JL, et al. 2018. *MNRAS* 480:5689–703
Holoien TWS, Huber ME, Shappee BJ, Eracleous M, Auchettl K, et al. 2019a. *Ap. J.* 880:120
Holoien TWS, Kochanek CS, Prieto JL, Grupe D, Chen P, et al. 2016a. *MNRAS* 463:3813–28
Holoien TWS, Kochanek CS, Prieto JL, Stanek KZ, Dong S, et al. 2016b. *MNRAS* 455:2918–35
Holoien TWS, Prieto JL, Bersier D, Kochanek CS, Stanek KZ, et al. 2014. *MNRAS* 445:3263–77
Holoien TWS, Vallely PJ, Auchettl K, Stanek KZ, Kochanek CS, et al. 2019b. *Ap. J.* 883:111
Hryniewicz K, Walter R. 2016. *Astron. Astrophys.* 586:A9
Hudec R, Sveda L, Pna L, Inneman A, Semencova V, Skulinova M. 2017. *Proc. SPIE Conf. Ser.* 10567:1056719
Hung T, Cenko SB, Roth N, Gezari S, Veilleux S, et al. 2019. *Ap. J.* 879:119
Hung T, Foley RJ, Ramirez-Ruiz E, Dai JL, Auchettl K, et al. 2020. *Ap. J.* 903:31
Hung T, Gezari S, Blagorodnova N, Roth N, Cenko SB, et al. 2017. *Ap. J.* 842:29
Irwin JA, Brink TG, Bregman JN, Roberts TP. 2010. *Ap. J. Lett.* 712:L1–4
Jiang N, Dou L, Wang T, Yang C, Lyu J, Zhou H. 2016. *Ap. J. Lett.* 828:L14
Jiang N, Wang T, Mou G, Liu H, Dou L, et al. 2019. *Ap. J.* 871:15
Jiang N, Wang T, Yan L, Xiao T, Yang C, et al. 2017. *Ap. J.* 850:63
Kajava JJE, Giustini M, Saxton RD, Miniutti G. 2020. *Astron. Astrophys.* 639:A100
Kara E, Dai L, Reynolds CS, Kallman T. 2018. *MNRAS* 474:3593–98
Kesden M. 2012a. *Phys. Rev. D* 85:024037
Kesden M. 2012b. *Phys. Rev. D* 86:064026
Khabibullin I, Sazonov S, Sunyaev R. 2014. *MNRAS* 437:327–37
Kobayashi S, Laguna P, Phinney ES, Mészáros P. 2004. *Ap. J.* 615:855–65
Kochanek CS. 2016. *MNRAS* 458:127–34
Kochanek CS, Shappee BJ, Stanek KZ, Holoien TWS, Thompson TA, et al. 2017. *Publ. Astron. Soc. Pac.* 129:104502
Komossa S, Greiner J. 1999. *Astron. Astrophys.* 349:L45–48
Komossa S, Zhou H, Wang T, Ajello M, Ge J, et al. 2008. *Ap. J. Lett.* 678:L13
Krolik J, Piran T, Svirski G, Cheng RM. 2016. *Ap. J.* 827:127
Law-Smith J, MacLeod M, Guillochon J, Macias P, Ramirez-Ruiz E. 2017. *Ap. J.* 841:132
Law-Smith JAP, Coulter DA, Guillochon J, Mockler B, Ramirez-Ruiz E. 2020. *Ap. J.* 905:141
Lei WH, Yuan Q, Zhang B, Wang D. 2016. *Ap. J.* 816:20
Leloudas G, Dai L, Arcavi I, Vreeswijk PM, Mockler B, et al. 2019. *Ap. J.* 887:218
Leloudas G, Fraser M, Stone NC, van Velzen S, Jonker PG, et al. 2016. *Nat. Astron.* 1:0002
Levan AJ, Tanvir NR, Cenko SB, Perley DA, Wiersema K, et al. 2011. *Science* 333:199
Lezhnin K, Vasiliev E. 2016. *Ap. J.* 831:84
Li LX, Narayan R, Menou K. 2002. *Ap. J.* 576:753–61
Lidskii VV, Ozernoi LM. 1979. *Sov. Astron. Lett.* 5:16–19
Lin D, Carrasco ER, Grupe D, Webb NA, Barret D, Farrell SA. 2011. *Ap. J.* 738:52
Lin D, Guillochon J, Komossa S, Ramirez-Ruiz E, Irwin JA, et al. 2017. *Nat. Astron.* 1:0033
Lin D, Maksym PW, Irwin JA, Komossa S, Webb NA, et al. 2015. *Ap. J.* 811:43
Liu FK, Zhou ZQ, Cao R, Ho LC, Komossa S. 2017. *MNRAS* 472:L99–103
Liu XL, Dou LM, Shen RF, Chen JH. 2019. *Ap. J.* Submitted. arXiv:1912.06081
Lodato G, King AR, Pringle JE. 2009. *MNRAS* 392:332–40
Lodato G, Rossi EM. 2011. *MNRAS* 410:359–67
Loeb A, Ulmer A. 1997. *Ap. J.* 489:573–78
Lu W, Kumar P, Evans NJ. 2016. *MNRAS* 458:575–81
MacLeod M, Guillochon J, Ramirez-Ruiz E. 2012. *Ap. J.* 757:134
MacLeod M, Guillochon J, Ramirez-Ruiz E, Kasen D, Rosswog S. 2016. *Ap. J.* 819:3
Magorrian J, Tremaine S. 1999. *MNRAS* 309:447–60
Maksym WP, Lin D, Irwin JA. 2014a. *Ap. J. Lett.* 792:L29
Maksym WP, Ulmer MP, Eracleous M. 2010. *Ap. J.* 722:1035–50
Maksym WP, Ulmer MP, Eracleous MC, Guennou L, Ho LC. 2013. *MNRAS* 435:1904–27
Maksym WP, Ulmer MP, Roth KC, Irwin JA, Dupke R, et al. 2014b. *MNRAS* 444:866–73

Maoz D. 2007. *MNRAS* 377:1696–710
Martin DC, Fanson J, Schiminovich D, Morrissey P, Friedman PG, et al. 2005. *Ap. J. Lett.* 619:L1–6
Mattila S, Pérez-Torres M, Efstathiou A, et al. 2018. *Science* 361:482–85
Metzger BD, Stone NC. 2016. *MNRAS* 461:948–66
Miller MC. 2015. *Ap. J.* 805:83
Milne PA, Brown PJ, Roming PWA, Bufano F, Gehrels N. 2013. *Ap. J.* 779:23
Milosavljević M, Merritt D. 2003. *Ap. J.* 596:860–78
Mockler B, Guillochon J, Ramirez-Ruiz E. 2019. *Ap. J.* 872:151
Nicholl M, Blanchard PK, Berger E, Gomez S, Margutti R, et al. 2019. *MNRAS* 488:1878–93
Nicholl M, Wevers T, Oates SR, Alexander KD, Leloudas G, et al. 2020. *MNRAS* 499:482–504
Nikołajuk M, Walter R. 2013. *Astron. Astrophys.* 552:A75
Palaversa L, Gezari S, Sesar B, Stuart JS, Wozniak P, et al. 2016. *Ap. J.* 819:151
Parkinson EJ, Knigge C, Long KS, Matthews JH, Higginbottom N, et al. 2020. *MNRAS* 494:4914–29
Pasham DR, Cenko SB, Levan AJ, Bower GC, Horesh A, et al. 2015. *Ap. J.* 805:68
Pasham DR, Remillard RA, Fragile PC, Franchini A, Stone NC, et al. 2019. *Science* 363:531–34
Pasham DR, van Velzen S. 2018. *Ap. J.* 856:1
Peterson BM, Ferland GJ. 1986. *Nature* 324:345–47
Phinney ES. 1989. Manifestations of a Massive Black Hole in the Galactic Center. In *The Center of the Galaxy*, ed. M Morris, vol. 136 of *IAU Symposium*
Piran T, Svirski G, Krolik J, Cheng RM, Shiokawa H. 2015. *Ap. J.* 806:164
Ramirez-Ruiz E, Rosswog S. 2009. *Ap. J. Lett.* 697:L77–80
Rees MJ. 1988. *Nature* 333:523–28
Reis RC, Miller JM, Reynolds MT, Gültekin K, Maitra D, et al. 2012. *Science* 337:949
Renzini A, Greggio L, di Serego Alighieri S, Cappellari M, Burstein D, Bertola F. 1995. *Nature* 378:39–41
Rosswog S, Ramirez-Ruiz E, Hix WR. 2009. *Ap. J.* 695:404–19
Roth N, Kasen D. 2018. *Ap. J.* 855:54
Roth N, Kasen D, Guillochon J, Ramirez-Ruiz E. 2016. *Ap. J.* 827:3
Roth N, van Velzen S, Cenko SB, Mushotzky RF. 2020. *Ap. J.* Accepted. arXiv:2008.11231
Ryu T, Krolik J, Piran T. 2020a. *Ap. J.* 904:73
Ryu T, Krolik J, Piran T, Noble SC. 2020b. *Ap. J.* 904:98
Saxton RD, Motta SE, Komossa S, Read AM. 2015. *MNRAS* 454:2798–803
Saxton RD, Read AM, Esquej P, Komossa S, Dougherty S, et al. 2012. *Astron. Astrophys.* 541:A106
Saxton RD, Read AM, Komossa S, Lira P, Alexander KD, Wieringa MH. 2017. *Astron. Astrophys.* 598:A29
Short P, Nicholl M, Lawrence A, Gomez S, Arcavi I, et al. 2020. *MNRAS* 498:4133
Stein R, van Velzen S, Kowalski M, Franckowiak A, Gezari S, et al. 2020. *New Astron.* Accepted. arXiv:2005.05340
Stone NC, Metzger BD. 2016. *MNRAS* 455:859–83
Stone NC, van Velzen S. 2016. *Ap. J.* 825:L14
Strubbe LE, Quataert E. 2009. *MNRAS* 400:2070–84
Strubbe LE, Quataert E. 2011. *MNRAS* 415:168–80
Syer D, Ulmer A. 1999. *MNRAS* 306:35–42
Tonry JL, Denneau L, Heinze AN, Stalder B, Smith KW, et al. 2018. *Publ. Astron. Soc. Pac.* 130:064505
Trakhtenbrot B, Arcavi I, Ricci C, Tacchella S, Stern D, et al. 2019. *Nat. Astron.* 3:242–50
Ulmer A. 1999. *Ap. J.* 514:180–87
van Velzen S. 2018. *Ap. J.* 852:72
van Velzen S, Farrar GR. 2014. *Ap. J.* 792:53
van Velzen S, Farrar GR, Gezari S, Morrell N, Zaritsky D, et al. 2011. *Ap. J.* 741:73
van Velzen S, Gezari S, Hammerstein E, Roth N, Frederick S, et al. 2021. *Ap. J.* 908:4
van Velzen S, Holoien TWS, Onori F, Hung T, Arcavi I. 2020. *Space Sci. Rev.* 216:124
van Velzen S, Mendez AJ, Krolik JH, Gorjian V. 2016. *Ap. J.* 829:19
van Velzen S, Stone NC, Metzger BD, Gezari S, Brown TM, Fruchter AS. 2019. *Ap. J.* 878:82
Wang J, Merritt D. 2004. *Ap. J.* 600:149–61

Wang T, Yan L, Dou L, Jiang N, Sheng Z, Yang C. 2018. *MNRAS* 477:2943–65
Wang TG, Zhou HY, Komossa S, Wang HY, Yuan W, Yang C. 2012. *Ap. J.* 749:115
Wevers T, Pasham DR, van Velzen S, Leloudas G, Schulze S, et al. 2019. *MNRAS* 488:4816–30
Wyrzykowski Ł, Zieliński M, Kostrzewa-Rutkowska Z, Hamanowicz A, Jonker PG, et al. 2017. *MNRAS* 465:L114–18
Yalinewich A, Guillochon J, Sari R, Loeb A. 2019. *MNRAS* 482:2872–77
Yang C, Wang T, Ferland GJ, Dou L, Zhou H, et al. 2017. *Ap. J.* 846:150
Yang CW, Wang TG, Ferland G, Yuan W, Zhou HY, Jiang P. 2013. *Ap. J.* 774:46
Yang Q, Shen Y, Liu X, Wu XB, Jiang L, et al. 2019. *Ap. J.* 885:110
Zauderer BA, Berger E, Soderberg AM, Loeb A, Narayan R, et al. 2011. *Nature* 476:425–28

Contents

Annual Review of Astronomy and Astrophysics

Volume 59, 2021